Evolution of Non-metallic Inclusions Through Processing in Ti-V Microalloyed 316L and Al-V Microalloyed 17-4PH Stainless Steels for Hipping Applications

MARÍA J. BALART, XINJIANG HAO, SAMUEL MARKS, GEOFF D. WEST, MARC WALKER, and CLAIRE L. DAVIS

Powders produced by air-melted gas atomization (AMGA) and vacuum induction gas atomization (VIGA) from Ti-V microalloyed 316L and Al-V microalloyed 17-4PH stainless steels along with their feedstock material and Hot Isostatically Pressed (HIP'd) products have been examined. Inclusion characteristics and development through process along with changes in grain size have been characterized. The main findings are that a thin oxide film forms on the powder surface, thicker for the 316L powder than the 17-4PH powder as indicated by XPS analysis of selected powder precursors, and large inclusions (predominantly oxides) are also observed on the 316L powder. This results in a high number of inclusions, including more complex two-phase inclusions, on the prior particle boundaries in the HIP'd material. Grain growth occurs during HIPping of the 316L powders with some evidence of inclusions locally pinning boundaries. In the vacuum-melted powder, smaller Ti-rich inclusions are present which give more grain boundary pinning than in the air-melted powder where Ti was lost from the material during melting. Consideration has also been made to determine the variation of Ti and V microalloying elements and residual Cu through processing. It was found that Ti was lost during air melting but partly retained after vacuum melting leading to the presence of fine and complex Ti-containing precipitates which provided grain boundary pinning during HIPping and heat treatment. V was retained in the melt by the use of both AMGA and VIGA processes, and therefore available for precipitation during HIPping. Residual Cu was retained during both air and vacuum melting and was associated with Mn S and Mn O S inclusions overwhelmingly outweighing that of Mn O inclusions in the two HIP'd 316L samples.

https://doi.org/10.1007/s11661-020-06010-w

I. INTRODUCTION

316L and 17-4PH stainless steels are versatile materials being used in many industrial sectors such as offshore, marine, aerospace, nuclear, chemical, and bioengineering due to their good combination of mechanical properties and corrosion resistance.[1] Recently, several investigations have highlighted the potential of HIP'd 316L steel for the fabrication of pressure retaining components for nuclear reactors.[2–5] Growth in the powder metallurgy sector[6–12] has led to a considerable increase in the complexity of alloys, products, and processing routes, in particular the metallic powder supply chain.[13]

One of the main factors to take into consideration in metallic powders is that most steel alloying elements such as Cr, Mn, Ti, V, Si, and Al are highly reactive to oxygen when exposed to air or other oxygen containing atmospheres and can spontaneously oxidize even under high vacuum conditions.[14] Metallic elements can also

MARÍA J. BALART is with the University of Warwick, WMG - Advanced Manufacturing and Materials Centre (AMMC), Coventry CV4 7AL, UK and also with the BCAST, Brunel University London, Uxbridge, Middlesex UB8 3PH, UK Contact e-mail: Maria.Balart@brunel.ac.uk XINJIANG HAO is with the University of Warwick, WMG - Advanced Manufacturing and Materials Centre (AMMC) and also with Liberty Powder Metals, Materials Processing Institute, Eston Road, Middlesbrough TS6 6US, UK. SAMUEL MARKS is with the University of Warwick, WMG - Advanced Manufacturing and Materials Centre (AMMC) and also with the Oxford Instruments NanoAnalysis, High Wycombe, Buckinghamshire HP12 3SE, UK. GEOFF D. WEST and CLAIRE L. DAVIS are with the University of Warwick, WMG - Advanced Manufacturing and Materials Centre (AMMC). MARC WALKER is with the Department of Physics, University of Warwick, Gibbet Hill Road, Coventry CV4 7AL, UK.

Manuscript submitted March 23, 2020.
Article published online October 12, 2020

spontaneously combine with sulfur. This can be typified by the Ellingham diagrams for oxides and sulfides.[15] Surface oxidation of the molten steel droplets is unavoidable during atomization as oxide films easily form at the free surface of liquid metal. Powder precursors from stainless steel can be produced by a wide range of gas atomization techniques and generally have a high surface purity, particularly for vacuum induction gas atomization (VIGA). However, the surfaces can become degraded when the unused powder is recycled after additively manufacturing (AM), for example, the formation of sub-micron-sized (< 200 nm) Cr-Mn-Si-rich oxide particulates has been reported on recycled VIGA powder after AM by electron beam melting (EBM) and laser sintering (LS) processing.[16] In addition, HIP'd 316L steel can contain endogenous oxidation products, along with deoxidation products, which mean that the steel product will contain a large number of non-metallic inclusions.[17,18] The presence of non-metallic inclusions can harmfully affect the mechanical and corrosion properties of the steel and are therefore important to characterize and control.

Q*uasi*-automated and automated SEM/EDS analyses have been extensively used among academia,[19–24] industry,[25–27] and other organizations[29] in the last few years for non-metallic inclusions characterization for clean steelmaking and quality control. In particular, SEM/EDS in conjunction with statistical data analysis has recently been proposed by Santecchia *et al.*[22] for evaluation and benchmarking aiming at standardization, quality control, and quality assurance.

Composition vs depth profile measurements on 316L powder surfaces were analyzed, in the 1980s, by Auger electron spectroscopy on water-atomized 316L powder[29] and, more recently, by XPS as exemplified in Reference 16. In the water-atomized case, it was found that Si has a higher affinity to oxygen than Cr at high melting temperatures as well as high mobility in the liquid melt, and preferably oxidizes and migrates to the surface of the liquid 316L steel.[29] These results were confirmed by Hedberg *et al.*[30] However, in the gas-atomized case of Reference 16, a very thin surface, iron oxide layer was formed in between the Cr-Mn-Si-rich surface oxide particulates. The very thin surface iron oxide layer was reported to be 2.9 nm in the as-atomized condition and 2.6 nm in the recycled powder condition.[16] Hedberg *et al.*[30] reported in the same study an Fe-rich layer, possibly Fe_2O_3, and that oxides on the surface of inert gas-atomized 316L powders were found to be enriched in Mn, Fe, and S nanoparticles (20 to 200 nm). As highlighted in their work,[30] the surface microchemistry and stability depend on the steel alloy composition and key process parameters which are explicitly the cooling rate during atomization, the type of atomization, and the oxygen concentration in the atomization atmosphere.

Cooper *et al.*[3–5,31] conducted comparative studies between forged and HIP'd 304L and 316L steels. The oxygen content in the 304L steel was 15 wt ppm in the forged material compared with 110 wt ppm in the powder sample and 120 wt ppm in the HIP'd sample.[3,31] The oxygen content in the 316L steel was 23 wt

Table I. Chemical Composition (Weight Percent) of the Investigated *Ti-V* Microalloyed 316L Steels

		B	Co	Cr	Cu	Mn	Mo	Ni	P	Si	V	W
Specification				16.0-18.0		2.00 max.	2.00–3.00	10.0–14.0	0.045 max.	0.75 max.		
Feedstock	AM	0.001	0.336	16.62	0.506	1.45	2.04	10.61	0.035	0.506	0.05	0.11
Powder	< 150 μm AMGA	< 0.02	0.35	17.14	0.49	1.26	2.12	10.78	0.038	0.45	0.06	0.08
Powder	106–150 μm^{XPS} VIGA	< 0.02	0.33	15.77	0.44	1.35	1.99	10.22	0.037	0.46	0.064	0.08
Powder*	15–45 μm^{XPS} VIGA	< 0.02	0.04	16.67	0.07	0.53	2.32	12.49	0.017	0.6	0.04	< 0.02
HIP'd	< 150 μm AMGA	< 0.02	0.36	16.71	0.50	1.07	2.08	11.36	0.041	0.36	0.07	0.10
HIP'd	106–150 μm VIGA	< 0.02	0.35	16.59	0.49	1.41	2.03	10.58	0.037	0.52	0.07	0.09

		Sn	Ta	Al	Ti	Nb	C	S	N	O	Fe
Specification							0.030 max.	0.03 max.	0.10 max.		bal.
Feedstock	AMGA	0.011		0.012	0.13	0.013	0.008	0.015	0.019		bal.
Powder	< 150 μm AMGA	< 0.02	< 0.02	< 0.05	< 0.02	< 0.02	0.0147	0.0142	0.0246	0.0355	bal.
Powder	106–150 μm^{XPS} VIGA	< 0.02	< 0.02	0.007	0.046	0.012	0.0118	0.0108	0.1143	0.0360	bal.
Powder*	15–45 μm^{XPS} VIGA	< 0.02	< 0.02		< 0.02	< 0.02	0.0241	0.0069	0.0887	0.0627	bal.
HIP'd	< 150 μm AMGA	0.015	< 0.02	0.005	< 0.005	< 0.005	0.0140	0.0148	0.0243	0.0665	bal.
HIP'd	106–150 μm VIGA	0.013	< 0.02	0.100	0.05	0.006	0.0112	0.0110	0.1051	0.0557	bal.

*Additional powdered steel sample not processed from the feedstock material of the present investigation.
^{XPS}Powdered steel samples analyzed by XPS.

Table II. Chemical Composition (Weight Percent) of the Investigated *Al-V*-Modified 17-4PH Steels

		B	Co	Cr	Cu	Mn	Mo	Ni	P	Si	*V*	W	Pb	Ca
Specification				15.00–17.50	3.00–5.00	1.00 max.		3.00–5.00	0.04 max.	1.00 max.				
Feedstock	VIM	0.0025	0.020	15.40	3.19	0.64	0.11	4.99	0.021	0.33	0.08	< 0.010	< 0.0005	0.0005
Powder	< 150 μm VIGA	< 0.02	0.02	15.44	3.06	0.51	0.12	5.03	0.026	0.51	0.08	< 0.02		
Powder	106–150 μm^{XPS} VIGA													
HIP'd	25–45 μm VIGA	< 0.02	0.03	15.78	3.11	0.62	0.12	5.06	0.026	0.33	0.08	0.0025		

		Sn	Ta	*Al*	Ti	Nb	Nb + Ta	C	S	N	O	Fe
Specification							0.15–0.45	0.07 max.	0.03 max.			bal.
Feedstock	VIM	0.005	< 0.010	0.032	< 0.010	0.29		0.04	0.0009	0.030	0.0010	bal.
Powder	< 150 μm VIGA	< 0.02	< 0.02	< 0.05	< 0.02	0.31		0.0406	0.0010	0.0351	0.0318	bal.
Powder	106–150 μm^{XPS} VIGA											
HIP'd	25–45 μm VIGA	< 0.0071	< 0.02	0.032	< 0.002	0.34		0.0420	0.0010	0.1759	0.0216	bal.

^{XPS}Powdered steel samples analyzed by XPS.

ppm in the forged material and ranged from 100 to 190 wt ppm in the HIP'd samples.[4,5] These values were lower than those in the powder and HIP'd steels of the present investigation, where purposefully enhanced oxygen contents in the powders, from storage and handling, were carried through into the HIP´d product to assess the non-metallic inclusions through processing. The grain boundary characterization and grain size in gas-atomized 316L austenitic stainless steel powders—AMGA (sieved to 25 to 45 and < 150 μm) and VIGA (sieved to 106 to 150 μm) and after HIP product fabrication—have been presented separately.[17,18] A preliminary comparison of the non-metallic inclusions in the HIP'd products was also made.[17,18]

An added challenge is that, in addition to oxidation, the control of tramp elements in steels is becoming more critical to meet the required steel quality as the demand for the use of scrap in steel manufacturing processes has increased significantly. In particular, there is an increased presence of Cu in scrap due to an increased presence in automotive scrap.[32] A residual Cu content in the base composition of 0.2 wt pct can impair the hot workability of the steel.[33] The presence of Cu in steel scrap can vary in the range between 0.1 and 0.3 wt pct.[33] Practical approaches to remove Cu from steel scrap have consisted of magnetic separation[33,34] following both shredding[33] or non-shredding.[34] In the former case, it can then be further processed by pyrometallurgy and hydrometallurgy.[33,35] In the latter case, the Cu-rich scrap product can be effectively sorted by hand pickers, sensor-based sorted, sold to specialized sorters,[34] or to copper smelters for Cu extraction.[34] In addition, direct sorting of stainless steel from scrap is also plausible.[36]

Cu has an ambivalent character in steels, it may be beneficial or deleterious. Deliberate additions of Cu are made to wrought steel products to enhance strength[37,38] and to improve the corrosion resistance.[39] Both 17-4 and 15-4 precipitation-hardening (PH) stainless steels are strengthened by Cu-rich precipitates in a martensitic matrix.[40] On the other hand, residual Cu can cause embrittlement which results from the physical mechanism in neutron-irradiated steel of matrix damage induced by point-defect Cu-rich clusters hardening[41,42] and hardening by copper precipitation.[42,43] In addition, residual Cu is deleterious to both hot ductility[44] and surface hot shortness.[45] From the point of view of Cu, Sn, and Ni impurities, Sn was found to enhance the Cu effect, while Ni had a counteracting action as exemplified by the Cu equivalent relationship: $Cu_{eq} = Cu + 8Sn - Ni$.[45] Note that, the residual levels are generally explicitly included in the materials specifications for aerospace applications. For example, in the IN718 alloy standard, the levels of residual elements (in wt ppm) are extremely low: 3Pb, 0.3Bi, and 3Se.[46] (as cited in Reference Kandasamy *et al.*[47]). Some ASTM MnMoNiCr grades plate and forging steels used for the manufacture of nuclear reactor pressure vessels have considered maximum Cu content values of 0.23–0.43[48] and 0-20-0.25 wt pct.[49] The ASTM A988/A988M-17[50] includes < 0.045P and < 0.03S wt pct residuals, and residual Cu in some of the steel grades. In contrast, the

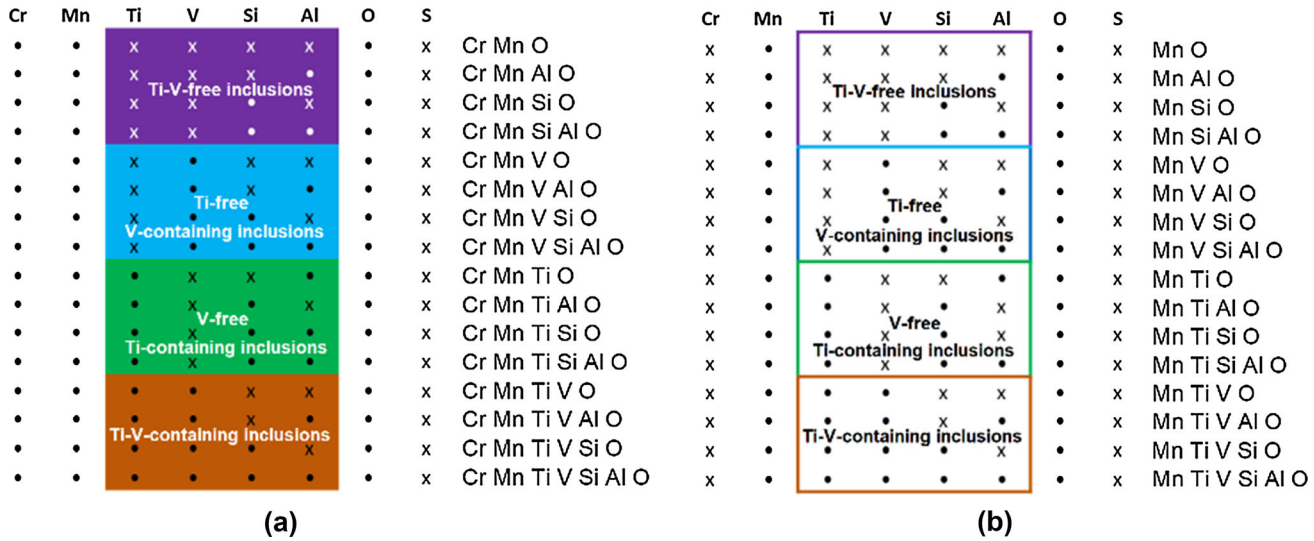

Fig. 1—Combination of elements in the inclusion classification showing elements being present above the matrix level (•) or not (x). This is depicted in two examples (*a*) and (*b*) of combinations of input elements (a) with Cr and (b) without Cr, and so on for oxysulfides. Note the color code (Color figure online).

specification maximum limit set by a supplier reported residual levels for 316L steel includes < 0.025P, < 0.01S, < 0.5Cu, < 0.1N, and < 0.1O wt pct.[51] There are no reports on where any Cu in the feedstock material is carried over into the powder and HIP products and whether it is associated with inclusions.

In this paper, we investigate the evolution of non-metallic inclusions through processing in Ti-V microalloyed 316L and Al-V microalloyed 17-4PH stainless steels for HIPping applications by means of various techniques: (i) automated SEM/EDS analysis for assessment of non-metallic inclusions and mapping of elements from feedstock to powder to HIP´d product; (ii) XPS analysis for comparison of surface oxides in selected powder precursors, and (iii) HAADF STEM in conjunction with EDX on two HIP´d 316L samples having two residual Ti levels (< 0.005 and 0.05 wt pct) from AMGA 316L (sieved to < 150 μm) and VIGA 316L (sieved to 106 to 150 μm), respectively. Special attention has been given to trace the variation of Ti and V microalloying elements and residual Cu through processing. Finally, we offer some broader reflections on powder metallurgy of 316L stainless steel in light of the evolution of non-metallic inclusions thought processing. We do so, by linking the Cu residual levels in 316L steel, scantly reported in the literature, with our case study to identify gaps leading to potential usage of steel scrap and standardization implications.

II. EXPERIMENTAL PROCEDURE

A. *Materials*

Feedstock, sieved powders, and HIP´d materials from both nitrogen atomized, AMGA Ti-V microalloyed 316L and VIGA Al-V microalloyed 17-4PH stainless steels as detailed in Tables I and II were supplied by Liberty Speciality Steels, UK. HIPping trials were carried out as follows. Mild steel canisters of 25 mm diameter and 200 mm length were filled with powder, vibrated to maximize compact density and vacuum degassed at room temperature. Subsequently, the canisters were sealed by hot crimping the evacuation tube. No gettering agent was used. The HIPping cycle consisted of simultaneous application of temperature at 4.64 K/s (5.5°C/min) and pressure at 0.009 MPa/s, HIP'd at 1393 K (1120 °C) and 103 MPa for 4 hrs in an argon atmosphere. After HIPping, the samples were solution annealed for 1 h at 1323 K (1050 °C) followed by water quenching. The canning material was removed by mechanical turning.

The chemical composition of the alloy steels investigated through processing as well as the minimum and maximum values as per steel specification are also given in Tables I and II. Note that, the residual levels of Cu and Sn are not quoted in the corresponding 316L and 17-4PH steel specifications. The use of Al deoxidation in the 316L steel resulted in some variation in residual Al levels (0.005 to 0.1 wt pct), while an Al microalloying addition led to two levels < 0.05 and 0.032 wt pct in the 17-4PH steel. The Ti content in the 316L steel varied from 0.13 wt pct in the feedstock to low residual levels of < 0.02 wt pct and < 0.005 wt pct in both AMGA powder and HIP'd product, respectively. While, Ti was partly retained in both the VIGA powder and HIP'd product to 0.046 wt pct and 0.05 wt pct, respectively, Ti microalloying element was at the residual levels (< 0.002 to < 0.02 wt pct) in the 17-4PH steel. Deliberate additions of Nb were made to the 17-4PH steel to act as a chemical carbon scavenger to suppress the formation of chromium carbides.[52] The levels of Nb microalloying element were residuals (< 0.005 to 0.013 wt pct) in the 316L steel. The microalloying element V varied between 0.04 and 0.07

Table III. Summary of Non-metallic Inclusions (mm^{-2}) for the 316L Steel Investigated

Non-metallic Inclusion Type	Feedstock	Powder < 150 μm	Powder 106–150 μm	HIP'd < 150 μm	HIP'd 106–150 μm
Ti N	39				
Ti N Mn S	178				
Mn Si Al O		1			
Mn Ti Si O		17			
Mn Ti Si Al O		33			
Ti Si Al O			11		
Cr Mn O				6740	5
Cr Mn Al O				0	6
Cr Mn Si O				335	7
Cr Mn Si Al O				1	1
Ti-V-free oxide inclusions				7076	19
Cr Mn V O				150	0
Cr Mn V Al O				0	0
Cr Mn V Si O				5	0
Cr Mn V Si Al O				1	0
Ti-free V-containing oxide inclusions				156	0
Cr Mn Ti O				9	1542
Cr Mn Ti Al O				2	868
Cr Mn Ti Si O				0	1378
Cr Mn Ti Si Al O				1	528
V-free Ti-containing oxide inclusions				12	4316
Cr Mn Ti V O				13	310
Cr Mn Ti V Al O				10	390
Cr Mn Ti V Si O				2	90
Cr Mn Ti V Si Al O				6	113
Ti-V-containing oxide inclusions				31	903
Cu O					21
Cu Mn O				42	2
Other Oxides				31	3523
Cr Mn S				2222	22
Cr Mn O S				19560	1
Cr Mn Al O S				2	4
Cr Mn Si O S				1400	14
Cr Mn Si Al O S				1	2
Ti-V-Free sulfide and oxysulfide Inclusions				23185	43
Cr Mn V O S				521	0
Cr Mn V Al O S				1	0
Cr Mn V Si O S				13	0
Cr Mn V Si Al O S				0	0
Ti-Free V-Containing oxysulfide Inclusions				535	0
Cr Mn Ti O S				22	840
Cr Mn Ti Al O S				3	510
Cr Mn Ti Si O S				10	1030
Cr Mn Ti Si Al O S					374
V-Free Ti-Containing oxysulfide Inclusions				35	2754
Cr Mn Ti V O				25	99

Table III. continued

Non-metallic Inclusion Type	Feedstock	Powder < 150 μm	Powder 106–150 μm	HIP'd < 150 μm	HIP'd 106–150 μm
Cr Mn Ti V Al O				13	242
Cr Mn Ti V Si O				2	56
Cr Mn Ti V Si Al O				4	80
Ti-V-Containing oxide Inclusions				44	477
Cu S					3
Cu Mn S				864	1802
Cu Mn O S				1027	3579
Other S				301	
Other O S					5689
Mn S	28			1212	
Mn O S				208	

Table IV. Summary of Non-metallic Inclusions (mm^{-2}) for the 17-4PH steel investigated

Non-metallic inclusion type	Feedstock	Powder < 150 μm	HIP'd 25 – 45 μm With Nb	HIP'd 25 – 45 μm Without Nb
Mn Ti Si Al O		10		
Cr Mn O			15	42
Cr Mn Al O			463	851
Cr Mn Si O			9	1
Cr Mn Si Al O			172	32
Ti-V-Free oxide Inclusions			659	926
Cr Mn V O			9	3
Cr Mn V Al O			78	10
Cr Mn V Si O			2	0
Cr Mn V Si Al O			74	1
Ti-Free V-Containing oxide Inclusions			163	
Cr Mn Ti O			0	0
Cr Mn Ti Al O			1	0
Cr Mn Ti Si O			0	0
Cr Mn Ti Si Al O			0	0
V-Free Ti-Containing oxide Inclusions			1	
Cr Mn Ti V O			0	0
Cr Mn Ti V Al O			0	0
Cr Mn Ti V Si O			0	0
Cr Mn Ti V Si Al O			0	0
Ti-V-Containing oxide Inclusions			0	
Cu O			842	1347
Cu Mn O			25	137
Other Oxides			581	1408
Cr Mn S			5	3
Cr Mn O S			12	39
Cr Mn Al O S			2	3
Cr Mn Si O S			1	1
Cr Mn Si Al O S			4	3
Ti-V-Free sulphide and oxysulfide Inclusions			24	49
Cr Mn V O S			9	0
Cr Mn V Al O S			1	1
Cr Mn V Si O S			1	0
Cr Mn V Si Al O S			3	0

Table IV. continued

Non-metallic inclusion type	Feedstock	Powder < 150 μm	HIP'd 25 – 45 μm With Nb	HIP'd 25 – 45 μm Without Nb
Ti-Free V-Containing oxysulfide Inclusions			14	1
Cr Mn Ti O S			0	0
Cr Mn Ti Al O S			0	0
Cr Mn Ti Si O S			0	0
Cr Mn Ti Si Al O S			0	0
V-Free Ti-Containing oxysulfide Inclusions			0	0
Cr Mn Ti V O			0	0
Cr Mn Ti V Al O			0	0
Cr Mn Ti V Si O			0	0
Cr Mn Ti V Si Al O			0	0
Ti-V-Containing oxide Inclusions			0	0
Cu S			15	112
Cu Mn S			24	85
Cu Mn O S	1		16	71
Other S				
Other O S				
Mn S	1			
Mn O S				

Table V. Number Density (mm^{-2}) of Cu-Containing Inclusions from the HIP'd 316L Steel in Table III

	HIP'd < 150 μm			HIP'd 106–150 μm				
Size (μm)	Cu Mn O	Cu Mn S	Cu Mn O S	Cu O	Cu Mn O	Cu S	Cu Mn S	Cu Mn O S
0–1	42	863	1019	17	2	3	1773	3482
1–2		0	8	4			29	86
2–3		1	0					10
3–4								1

Table VI. Number Density (mm^{-2}) of Cu-Containing Inclusions from the HIP'd 17-4PH 25–45 μm Sample in Table IV

	HIP'd < 150 μm					HIP'd 106–150 μm				
Size (μm)	Cu O	Cu Mn O	Cu S	Cu Mn S	Cu Mn O S	Cu O	Cu Mn O	Cu S	Cu Mn S	Cu Mn O S
0–1	839	22	15	24	14	1343	132	112	84	64
1–2	3	3			2	4	5		1	6
2–3										1

wt pct in the 316L steel and 0.08 wt pct V in the 17-4PH steel.

The C and S contents of the samples were determined using an Eltra™ CS-2000 carbon/sulfur analyzer equipped with a high-frequency induction furnace for the air-melted powder and by LECO™ for the VIGA powder. The N and O contents of the samples were analyzed by LECO™. The other elements were analyzed by inductively coupled plasma optical emission spectrometry (ICP-OES).

B. *Characterization Techniques*

1. *SEM*

SEM backscattered electron imaging (BSEI) and EDS were carried out using a Versa 3D dual-beam SEM operating at 10 kV. Elemental analyses and mappings were processed using the Aztec OI software feature that integrates EDS analysis software with an XMax 80 SDD (Silicon Drift Detector) detector. BSEIs in conjunction with EDS were used to quantify the inclusion size

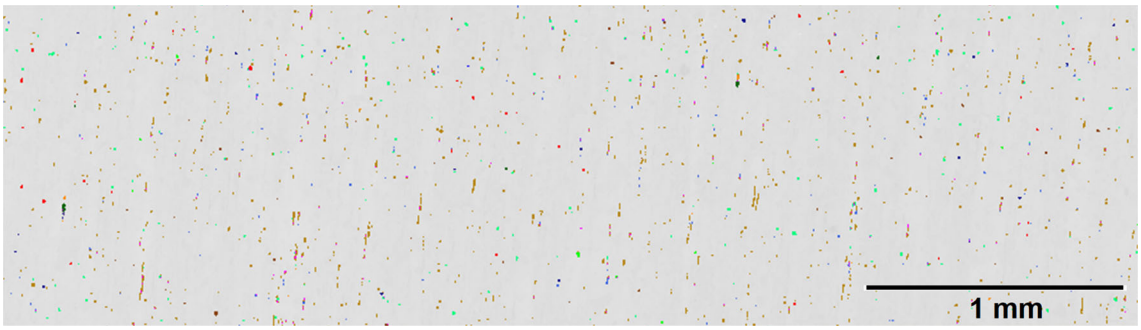

Fig. 2—Inclusion map for the 316L steel feedstock.

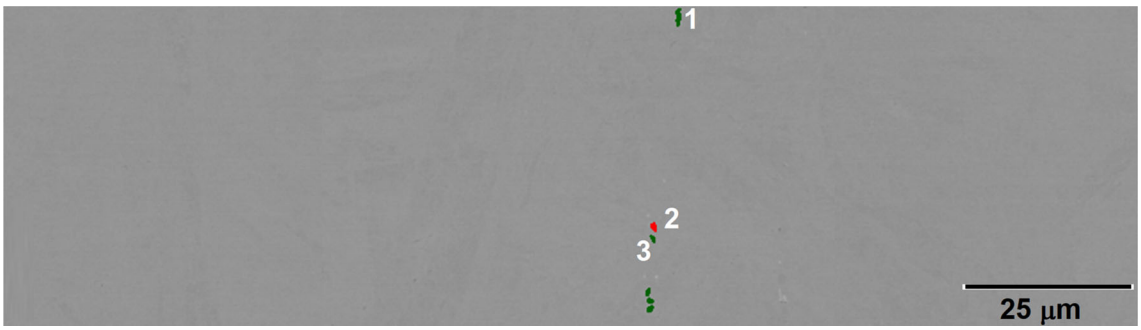

Fig. 3—Phase analysis for the 17-4PH steel feedstock showing Cr-rich (green 1 and 3) and Cr-Nb-rich (red 2) phases (Color figure online).

Table VII. EDS Analysis (Weight Percent) from the Phases in Fig. 3

Phase	Fe	Cr	Ni	Cu	Nb	Si	C
1	60.3 ± 0.5	34.9 ± 0.4	2.8 ± 0.3	1.9 ± 0.3			
2	58.8 ± 0.5	35.4 ± 0.4	2.3 ± 0.3	1.7 ± 0.3	1.3 ± 0.3	0.3 ± 0.1	
3	58.1 ± 0.6	35.7 ± 0.4	1.9 ± 0.3	1.2 ± 0.3			3.1 ± 0.6

(maximum dimension), number density and type on feedstock, and HIP'd product both on polished cross-sections and on polished powders, which required cold mounting and Au sputtering in an Agar auto sputter coater, using a setting of 40 mA, for 30 seconds. Preliminary EDS analysis of inclusions has confirmed the presence of elements to be included in our choice of classification to be input hierarchically in descending elemental content as established in the Aztec OI software. First, inclusions were categorized in two groups: with and without Cu. Second and for each of the two groups, inclusions were divided into four groups (oxysulfides, oxides, sulfides, and without both oxygen and sulfur) to analyze combinations of Cr and/or Mn with oxysulfides, oxides, sulfides, and without both oxygen and sulfur for combinations of 4-element subset (Ti V Si Al). In summary, combinations of 4-element subsets (Cr Mn O S) (Ti V Si Al) of an 8-element set were determined as illustrated in Figure 1. Other particular elements present in the analysis of a feature are also included in the EDS spectrum for later classification, for example, elements arising from cross-contamination and other residuals. An exemplification of nitrogen containing inclusions has been classified for combinations of (Mn Ti) or Ti with and without V subclasses with (N O S), (N S), and (O S).

2. *X-ray photoelectron spectroscopy (XPS)*

X-ray photoelectron spectroscopy (XPS) data were acquired using a Kratos Axis Ultra DLD spectrometer. The powders were mounted on to a sample bar using electrically conductive carbon tape and loaded in to the vacuum system. After pumping down, the samples were transferred to the analysis chamber (base pressure 1×10^{-10} mbar) and illuminated with an AlKα X-ray source ($h\nu = 1486.7$ eV). The photoelectrons were collected in a hemispherical analyzer from an area of 300 $\mu m \times 700$ μm on the sample surface. The binding energy scale of the spectrometer was calibrated using the Ag 3d and Fermi edge positions acquired from a clean polycrystalline Ag surface prior to the experiments. Survey spectra were recorded with a pass energy of 160 eV (resolution approximately 2 eV), while core-level spectra were recorded at a pass energy of 20 eV (resolution approximately 0.4 eV). XPS data were acquired from the samples at normal emission in the as-received

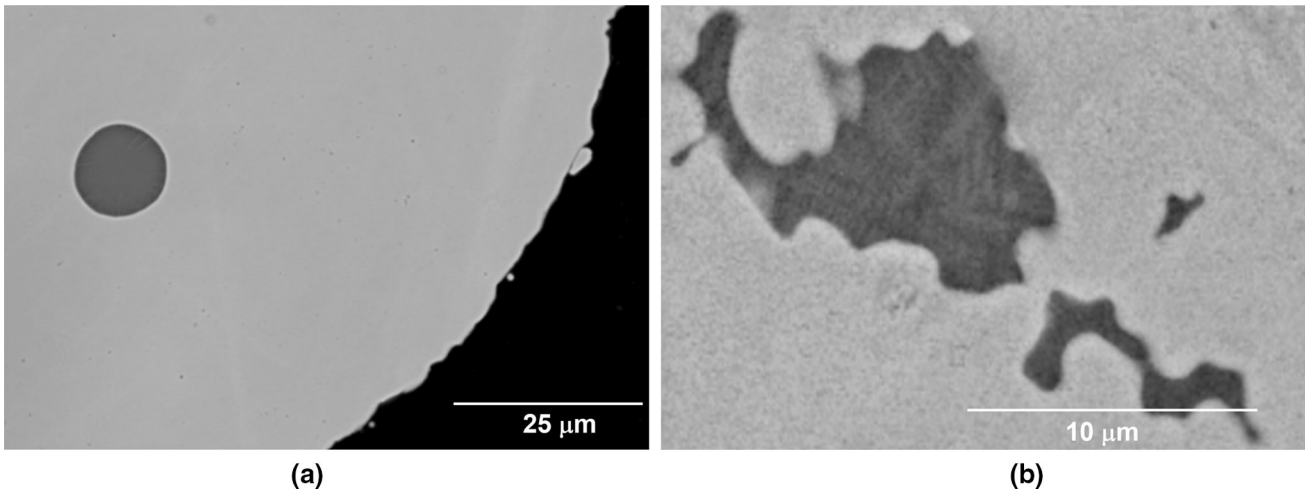

Fig. 4—Inclusion analysis for the AMGA 316L powder < 150 μm showing (*a*) globular and (*b*) dendritic morphologies.

Table VIII. EDS Analysis (Weight Percent) from the Inclusions in Fig. 4

	Mn	O	Cr	Si	C	Ti	Fe	Al	Ni
(a)	23.2 ± 0.6	23.2 ± 1.0	13.9 ± 0.4	11.5 ± 0.3	9.3 ± 1.4	8.5 ± 0.3	7.6 ± 0.4	1.5 ± 0.2	1.3 ± 0.2
(b)	20.3 ± 0.6	23.4 ± 1.1	11.1 ± 0.4	7.6 ± 0.2	12.7 ± 1.3	11.6 ± 0.3	9.0 ± 0.4	1.1 ± 0.1	1.4 ± 0.2

condition and following Ar^+ sputtering using an incident ion beam energy of 4 keV for 15 minutes with an angle between the sample surface and the ion beam of 45°. The resulting spectra were analyzed using the CasaXPS package[53] (version 2.3.19), using mixed Gaussian–Lorentzian (Voigt) lineshapes, asymmetry parameters where appropriate, and Shirley backgrounds.

3. *TEM*

TEM samples from the AMGA HIP'd 316L < 150 μm and VIGA HIP'd 106 to 150 μm products were prepared using focused ion beam (FIB) lift-out techniques in a Scios dual-beam FIB-SEM and were examined in an FEI Talos F200X S/TEM equipped with a Super X 4-quadrant X-ray detector, operating at 200 kV. TEM samples were attached to a Cu FIB TEM grid.

III. RESULTS

BSEI and EDS identified single and multi-phase inclusions, for both feedstock and HIP'd 316L steel conditions, while discrete phase inclusions were identified for the 316L powders. BSEI and EDS for the feedstock, powder, and HIP'd 17-4PH steel conditions identified not only non-metallic inclusions in all three samples, but also oxygen-free phases. Non-metallic inclusions for the 17-4 PH steel were present in much lower amounts than the corresponding feedstock, powder, and HIP'd 316L steel conditions. They were also found as single and multi-phase inclusions, for both feedstock and HIP conditions, while discrete single-phase inclusions were identified for the powders.

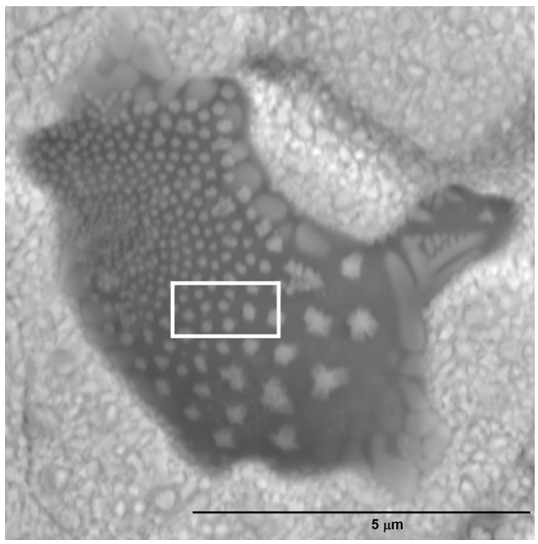

Fig. 5—Mn-Ti-(V)-Si-Al-containing oxide particulate on the powder surface from the VIGA 316L 106 to 150 μm sample.

Histograms of the inclusion number density through processing from the feedstock to powder to the HIP'd product are plotted in supplementary Figure S-1, for the 316L steel, and in supplementary Figure S-2, for the 17-4PH steel (refer to electronic supplementary material). The variation of the number density of inclusion types through processing for the two steels are summarized in Tables III and IV. The number density of the Cu-containing inclusions for all the three HIP'd samples are summarized in Tables V and VI.

Table IX. EDS Analysis (Weight Percent) from the Inset in Fig. 5

Mn	O	Si	Ti	Cr	N	C	Fe	Al	S	V	Mo
29.0 ± 0.3	23.9 ± 0.3	12.2 ± 0.1	10.9 ± 0.1	9.4 ± 0.1	7.2 ± 0.5	2.3 ± 0.1	2.1 ± 0.2	1.9 ± 0.0	1.0 ± 0.1	0.1 ± 0.1	0.0 ± 0.2

A. *316L and 17-4PH Stainless Steel Feedstocks*

An automated BSE image of the inclusions for the 316L steel feedstock is shown in Figure 2. The main phases identified in the 316L feedstock were Al_2O_3, MnS, and (Ti,V)(C,N) as single-phase inclusions or as part of multi-phase inclusions which included the following four main combinatory types: Al_2O_3/MnS; (Ti,V)(C,N)/Al_2O_3; (Ti,V)(C,N)/MnS; and (Ti,V)(C,N)/Al_2O_3/MnS.

An automated BSE image for the 17-4PH steel feedstock is shown in Figure 3. Oxygen-free phases were found to be darker with respect to the steel matrix in the 17-4PH steel feedstock. Those darker segregated second phases consisted of Cr-rich, low-Cu with or without (more frequent) Nb. Three examples from Figure 3 are given in Table VII.

B. *316L and 17-4PH Stainless Steel Powders*

The majority of non-metallic inclusions in the 316L powder were present as individual, single-phase particles of largely globular morphology (Figure 4(a) and Table VIII), but isolated inclusions of dendritic morphology were also observed (Figure 4(b) and Table VIII). Those are (i) predominantly of a Mn-Ti-Si-Al-containing oxide type followed by Mn-Ti-Si-containing oxides for the 316L < 150 μm powder (supplementary Figure S-1(b)) and (ii) predominantly of a Ti-Si-Al-containing oxide type followed by other oxides (such as Mn-Ti-Al-containing oxides and Ca-containing oxides), and then in the same ranking order by Mn-Ti-Si-containing oxides and Mn-Ti-Si-Al-containing oxides for the 316L 106 to 150 μm powder (supplementary Figure S-1(c)). Figure 5 shows a coarse Mn-Ti-(V)-Si-Al-containing oxide particulate on the surface of a VIGA powder 316L 106 to 150 μm sample. Its EDS analysis is given in Table IX.

The main inclusion type for the VIGA 17-4PH < 150 μm sample was found to be the same as that for the AMGA 316L < 150 μm sample: Mn-Ti-Si-Al-containing oxide inclusions (supplementary Figures S-2(b) *c.f.* S-1(b)). The chemical composition values for the Mn-Ti-Si-Al-containing oxide inclusions case were in the range (8.46 to 21.20)Cr-(2.60 to 18.04)Mn-(3.26 to 17.00)Si-(0.38 to 6.30)Al-(0.34 to 3.61)Ti (wt pct).

Survey spectra were acquired from the three powders in the as-received condition and, as shown in supplementary Figure S-3, revealed the presence of many different elements within the typical sampling depth of XPS (5 to 10 nm). Table X shows the atomic concentrations of the different elements detected after analysis of core-level spectra which were subsequently acquired (supplementary Figures S-4 to S-11). Table XI shows the relative amounts of Fe, FeO, and Fe_2O_3 in the near-surface region. Table XII summarizes the metallic elements and compounds for the three powders.

C. *HIP'd 316L and 17-4PH Stainless Steels*

Inclusion maps, examples of specific inclusions and their EDS analysis from the HIP'd samples consolidated from the 316L < 150 μm powder are shown in Figure 6

Table X. Total Elemental Compositions (Atomic Percent) of the Three Powders Studied in this Investigation, Before and After Ar^+ Sputtering at 4 keV

Sample	State	C	O	P	Cr	Ni	Si	Mn	Ti	Fe	Mo	Cu	Sn	V	Nb	N	Na
316L 106–150 μm	as-received	30.0	52.7	0.0	2.0	0.9	2.8	4.2	1.1	6.0	0.4	0.0	0.0	0.0	0.0	0.0	0.0
316L 106–150 μm	sputtered	27.6	50.5	0.0	2.9	1.4	2.7	4.6	1.3	8.6	0.5	0.0	0.0	0.0	0.0	0.0	0.0
316L 15–45 μm	as-received	28.6	53.7	0.0	2.0	0.7	6.3	3.2	0.0	5.2	0.4	0.0	0.0	0.0	0.0	0.0	0.0
316L 15–45 μm	sputtered	26.8	52.5	0.0	2.7	0.7	5.9	3.6	0.0	7.4	0.4	0.0	0.0	0.0	0.0	0.0	0.0
17-4PH 106–150 μm	as-received	24.0	50.5	3.0	1.0	0.1	3.4	0.0	0.0	9.7	0.0	6.6	0.1	0.0	0.7	0.5	0.5
17-4PH 106–150 μm	sputtered	18.9	26.9	2.1	5.6	1.9	3.6	0.0	0.0	33.9	0.0	5.2	0.1	0.0	0.7	1.1	0.0

Table XI. Relative Abundancies of Fe(0), Fe_2O_3, and FeO Observed in the Three Steel Powders, Measured in the As-Received Condition and After Ar^+ Sputtering at 4 keV

Sample	State	Metallic Fe(0)	Fe_2O_3	FeO
316L 106–150 μm	as-received	13.5	63.7	22.9
316L 106–150 μm	sputtered	8.9	14.6	76.5
316L 15–45 μm	as-received	7.0	93.0	0.0
316L 15–45 μm	sputtered	5.3	34.3	60.4
17-4PH 106–150 μm	as-received	8.1	27.3	64.7
17-4PH 106–150 μm	sputtered	80.9	0.0	19.1

and Table XIII and from the 316L 106 to 150 μm powder are shown in Figure 7 and Table XIV. BSEI and EDS analyses of a coarse, complex, two-phase inclusion are shown in Figure 8 and Table XV for the former case and in Figure 9 for the latter case. AMGA HIP'd 316L < 150 μm and VIGA HIP'd 106 to 150 μm samples were also characterized by TEM to confirm the presence or absence of Ti-containing precipitates. HAADF-STEM images and the corresponding EDAX elemental maps are shown in Figures 10 and 11.

An automated BSE image for the HIP'd 17-4PH 25 to 45 μm sample is shown in Figure 12. Oxygen-free phases were found to have a white contrast phase in BSEI, with the majority of the cases being Nb-rich (red), for example, 37.8Nb-27.7Cr-4.9N-2.0V-1.2Cu, but with some examples being Cu-rich (blue) 62.5Cu-rich, Figure 12, (as per atomic number Z-contrast 92.906 Nb, 63.546 Cu, and 55.845 Fe molar weight). Histograms of the number density of those white contrast phases are plotted in supplementary Figure S-13. It can be seen that the majority of the white contrast phase was Nb V Cr Cu (N) (11944 mm^{-2}), followed in decreasing order by Nb Cr (Cu V N) (414 mm^{-2}); V-free, low Cu (0.6 to 3.6 wt pct) (377 mm^{-2}), and Cu-rich (4 to 45.6 wt pct) (131 mm^{-2}). It can also be seen that oxidation did not generally occur, with the exception of the some Nb-Cr-Mn-containing (103 mm^{-2}) and Cu-rich (5 out of 131 mm^{-2}) phases (Table XVI).

IV. DISCUSSION

A. *316L and 17-4PH Stainless Steel Feedstocks*

The multi-phase inclusions identified for 316L feedstock are consistent with high melting point Al_2O_3 inclusions acting as nucleation sites for MnS and (Ti,V)(C,N) inclusions and also MnS inclusions precipitating on the pre-existing Al_2O_3 and/or (Ti,V)(C,N).[54] The 17-4PH steel feedstock had relatively low levels of 0.0009S-0.0010O-0.030N (wt pct) (Table II) and had a significantly lower number density of inclusions than the 316L feedstock (Figure 3 *c.f.* Figure 2 and supplementary Figure S-2(a) *c.f.* Figure S-1(a)).

B. *316L and 17-4PH Stainless Steel Powders*

Inclusions in the 316L powder were predominantly Mn-Ti-Si-Al-containing oxides inside the powder particles (Figure 4 and Table VIII), however, they were also observed on the surface of powder particles (Figure 5 and Table IX). Some examples of exogenous Ca-containing oxide inclusions were seen in the 316L steel, which could have arisen from trapped slag or refractories in the melt, such as calcium aluminates and silica, rather than cross-contamination of powder precursors during powder production, handling, and processing.[22,55,56]

Hryha *et al.*[16] reported nano-sized Cr-Mn-Si-rich surface oxide particulates in 316L to be very fine (~ 10 nm) in the as-atomized condition and relatively coarse, up to 200 nm, in powder recycled after AM by EBM and LS processing from powder precursors produced by VIGA. Experimental observations in another study[57] showed evidence that a mixture of SiO_2 and $MnCr_2O_4$ particles can form on the surface of gas-atomized 316L in powder recycling after AM by laser powder bed fusion processing. Coarse Mn-Ti-Si-Al-containing oxide inclusions in the 316L powder of the present investigation were found to be micron-sized and non-Cr-rich (see EDS analysis in Figures 4 and 5), indicating that Cr enrichment in the abovementioned particles of up to 200 nm in size could have occurred as a result of powder recycling after AM by EBM and LS processing.

Table XII. XPS Summary of Species for the Three Powders Studied in this Investigation, Before and After Ar^+ Sputtering at 4 keV

Sample	Metallic Elements	Compounds
316L 106–150 μm	Fe(0), Cr(0), Si(0), Mo(0), Ni(0), Mn (0), Ti(0)	FeO, Fe_2O_3, Cr(III), SiO, SiO_2, MoO_3, Ni(II), MnO, TiO_2
316L 15–45 μm	Fe(0), Cr(0), Si(0), Mo(0), Ni(0), Mn (0)	FeO, Fe_2O_3, Cr(III), SiO, SiO_2, MoO_3, Ni(II), MnO
17-4PH 106–150 μm	Fe(0), Cr(0), Si(0), Sn(0), Nb(0), P(0), and Cu(0) after Ar^+ sputtering.	FeO, Fe_2O_3, Cr(III), SiO, SnO/SnO_2, NbO_2, NbC/NbN, phosphates, Cu(II) in the as-received condition, Cu_2O after Ar^+ sputtering

Similar to the feedstock compared above, the number density of inclusions for the VIGA 17-4PH < 150 μm sample was also significantly lower than that for the AMGA 316L < 150 μm sample (supplementary Figure S-2(b) *c.f.* Figures S-1(b) and (c)), despite its relatively high oxygen level 0.0010S-0.0318O-0.0351N (wt pct) (Table II), suggesting that in the VIGA 17-4PH < 150 μm sample, oxygen was mainly present in the form of surface oxides as the feedstock had only 10 wt ppm O.

From a comparative study of non-metallic inclusions in 17-4PH powder and after being additively manufactured by selective laser melting, Sun *et al.*[19] reported the chemical composition (in wt pct) by TEM-EDXS in powder to be 14.2Cr-21.3Mn-9.7Al-22.7Si-32.1O for a large micron-sized inclusion. In the same study, Sun *et al.*[19] also reported that the ASTM A564 or AMS 5643 for 17-4PH specification do not include microalloying elements such as Ti, Al, and V, and therefore pointed out to an exogenous origin for those Al-containing inclusions, possibly arising from melt-crucible or melt-nozzle interactions during gas atomization. In contrast, the VIGA 17-4PH steel in the present investigation was Al- and V-doped (not Ti-doped) and had a lower number density of inclusions in the powder (supplementary Figure S-2(b)) than that reported in the work by Sun *et al.*,[19] in which the 17-4PH steel powder had an increased 0.0030S-0.046O-0.11N content (wt pct).

C. *XPS Analysis*

From the survey spectra in supplementary Figure S-3 and Table X, it is immediately clear from these data that Cu is only present near the surface of the 17-4PH 106 to 150 μm powder, with the two 316L powders not exhibiting the characteristic Cu $2p_{3/2}$ component in the region of 932 eV, as shown in supplementary Figures S-3 and S-4.

The high-resolution spectra acquired from the Fe $2p_{3/2}$ region of each sample before and after Ar^+ sputtering are shown in supplementary Figure S-5, with the work of Biesinger and co-workers used as the basis for analysis of these data.[58] As detailed in Table X, the total Fe content increased in all three samples following sputtering, indicating that surface contamination and other overlying material had been removed during this process. While the change was discernible in both 316L powders, the increase in total Fe observed was significantly greater in the 17-4PH powder, indicating that Fe and the associated oxides are closer to the surface of this particular powder and hence more exposed to the ion beam.

Analysis of the Fe $2p_{3/2}$ core-level spectra revealed the presence of metallic Fe, FeO, and Fe_2O_3 in the near-surface region. Table XI shows that the relative amount of Fe_2O_3 is reduced during sputtering in all three cases, suggesting that it is located at the surface. Interestingly, sputtering the 17-4PH sample also removes FeO and reveals more metallic Fe(0), whereas both 316L powders see an increase in the relative

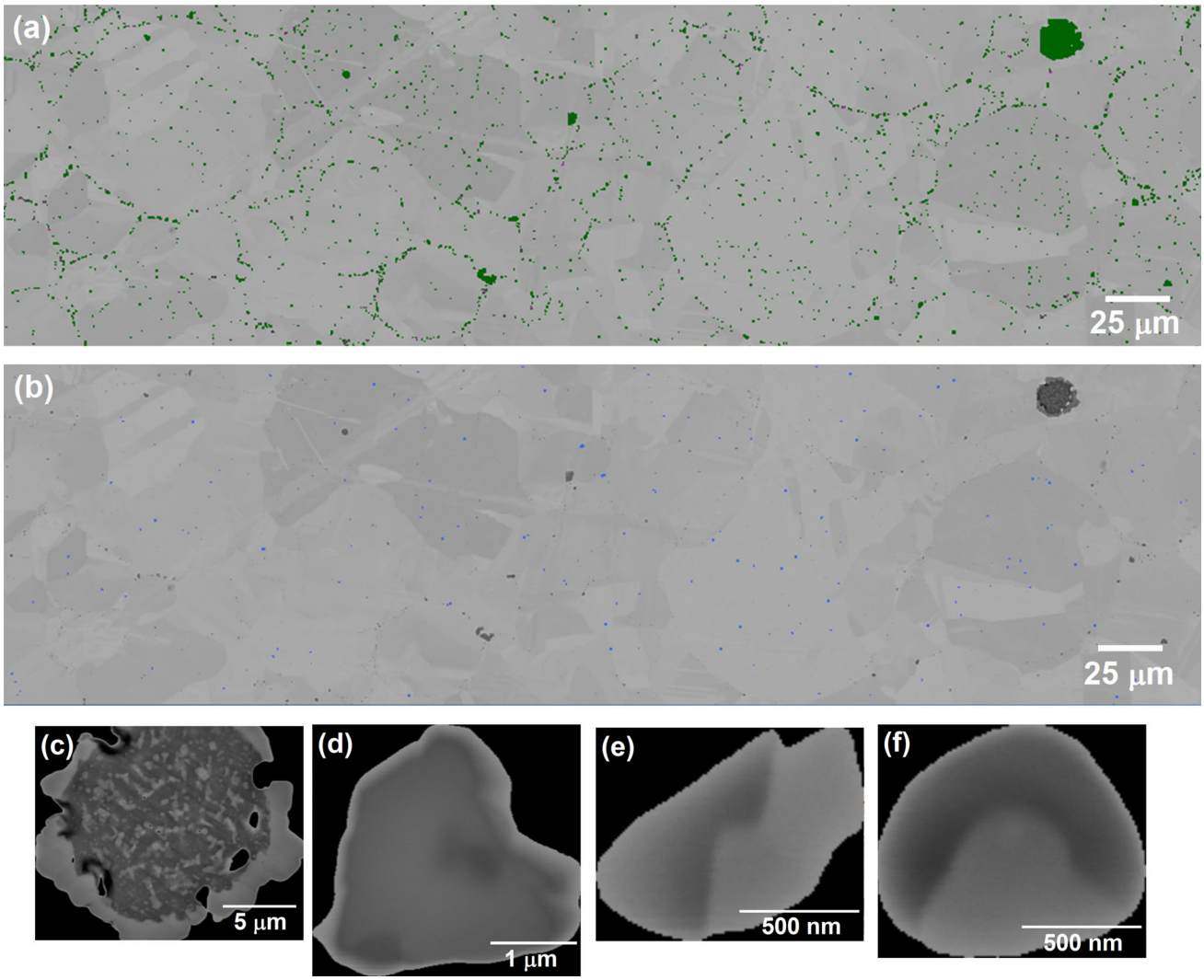

Fig. 6—Inclusion maps for the HIP'd 316L < 150 μm sample showing (*a*) Cr-containing inclusions; (*b*) Cu-containing inclusions; and examples of specific inclusions: (*c*) a Cr-Mn-Ti-V-Si-Al-(Ca)-containing oxide inclusion; (*d*) a Cr-Mn-Ti-V-Si-containing oxide inclusion; and (*e*) and (*f*) Cu Mn O S inclusions.

amount of FeO after sputtering. Again, this indicates a thicker Fe_2O_3 layer on the surface of the 316L powders.

The base composition of all three powders contains detectable amounts of Mo, 1.99 wt pct in 316L 106 to 150 μm, 2.32 wt pct in 316L 15 to 45 μm and 0.12 wt pct in 17-4PH. Hryha *et al.*[16] and Leicht *et al.*[59] proposed that Mo and Ni are both found in the metallic state in 316L powders, and to test this hypothesis high-resolution spectra of the Mo 3*d* and Ni 2*p* regions were acquired from the 316L powders as shown in supplementary Figure S-6. Note that the intensity from the as-received 17-4PH powder in the Ni 2*p* region was too low to accurately fit, and there was no evidence of the presence of Mo whatsoever. However, the data from the 316L powders were of sufficient quality to enable observation of both metallic and oxidized components in both elements. In the Mo 3*d* region, the metallic Mo(0) components were observed at 227.3 and 230.5 eV in the 316L 106 to 150 μm powder, with corresponding peaks recorded at 227.8 and 231.0 eV in the 316L 15 to

Table XIII. EDS Analysis (Weight Percent) from the Inclusions in Fig. 6

	O	Mn	Cr	Si	Fe	Ni	Al	Ti	V	Ca	S	Cu
(c)	27.8 ± 0.4	27.0 ± 0.3	22.2 ± 0.3	10.2 ± 0.1	10.1 ± 0.2	1.1 ± 0.1	0.8 ± 0.1	0.3 ± 0.1	0.3 ± 0.1	0.2 ± 0.1		
(d)	20.1 ± 0.6	24.5 ± 0.4	35.8 ± 0.5	1.2 ± 0.1	14.0 ± 0.4	1.3 ± 0.2		2.4 ± 0.1	0.6 ± 0.1			
(e)	4.8 ± 0.4	8.3 ± 0.3	18.3 ± 0.3		55.8 ± 0.5	8.0 ± 0.3					3.8 ± 0.2	1.0 ± 0.3
(f)	8.8 ± 0.5	12.5 ± 0.3	25.3 ± 0.4		43.6 ± 0.5	6.0 ± 0.3					3.0 ± 0.1	0.9 ± 0.3

45 μm case. An additional doublet at 232.2/232.3 and 235.3/235.4 eV was required in order to fully replicate the experimental data, corresponding to MoO_3 in a roughly equal quantity compared to Mo(0). This suggests a layer of MoO_3 on top of the Mo(0). A similar situation was observed in the Ni $2p_{3/2}$ region, where metallic Ni(0) presented a single component at 852.7/852.8 eV and a series of peaks corresponding to Ni(II) environments from the work of Biesinger[58] were required to replicate the data.

Due to the Ni and Cu contents of the 17-4PH powder, it was not possible to accurately fit the Mn 2*p* spectrum from this sample. However, MnO was observed in both 316L powders, while NbO_2 and NbC/NbN were detected in the Nb 3*d* region of the 17-4PH sample, as shown in supplementary Figure S-7. The observation of Mn oxides is again similar to the results of Leicht *et al.*[59] and Hryha *et al.*[16]

Potentially important impurities including Ti, Sn, P, and Cu, which may influence various properties of the steel, were detected using ICP and/or XPS. A Ti content of 0.046 wt pct was measured in ICP for the 316L 106 to 150 μm powder, compared to < 0.02 wt pct for the other two powders, corroborated in Table X which illustrates that the 316L 106 to 150 μm powder also had the highest Ti concentration in XPS, confirming that the Ti is partly retained during the manufacturing of the 316L 106 to 150 μm powder. Examining the Ti 2*p* region more closely, as shown in supplementary Figure S-8, contributions from both metallic Ti and TiO_2 were observed in the 316L 106 to 150 μm powder.

It is, however, of interest to note that despite all the three steel powder conditions having a Sn content in the base composition of < 0.02 wt pct (arising from feedstock steels having a low Sn content of 0.011 wt pct for the 316L 106 to 150 μm sample and a very low Sn content of 0.005 wt pct for the 17-4PH sample), the Sn 3*d* peak was only present in the 17-4PH 106 to 150 μm sample, with the peak positions indicative of Sn oxides, as shown in supplementary Figure S-9. The same trend was observed for P, with only the 17-4PH powder containing a concentration above the XPS detection limit, see Table X. The data in the P 2*p* region were rather noisy and overlap with the Cu 3*s* photoemission, but suggested the existence of elemental phosphorus and phosphates. This again corresponds with the iron oxide layer being very much thinner for the 17-4PH 106 to 150 μm case than the other two steels. In agreement with the XPS results reported by Heiden *et al.*[57] on 316L powder feedstock both in the as-received condition and after being reused in the laser bed fusion process, Sn and Cu were not detected by XPS on the surface of the two 316L powders of the present investigation. These findings, however, differed from those published earlier (having residual levels of 0.086 wt pct Cu and < 0.005 wt pct Sn) in that Cu and Sn (as well as S) were detected on the surface of fine (< 28 μm) and coarse (250 to 350 μm) martensitic stainless steel powders by the use of various spectroscopy techniques, including XPS, AES, and SIMS.[60]

Returning to the Cu content of the 17-4PH powder, the Cu $2p_{3/2}$ region was collected both before and after

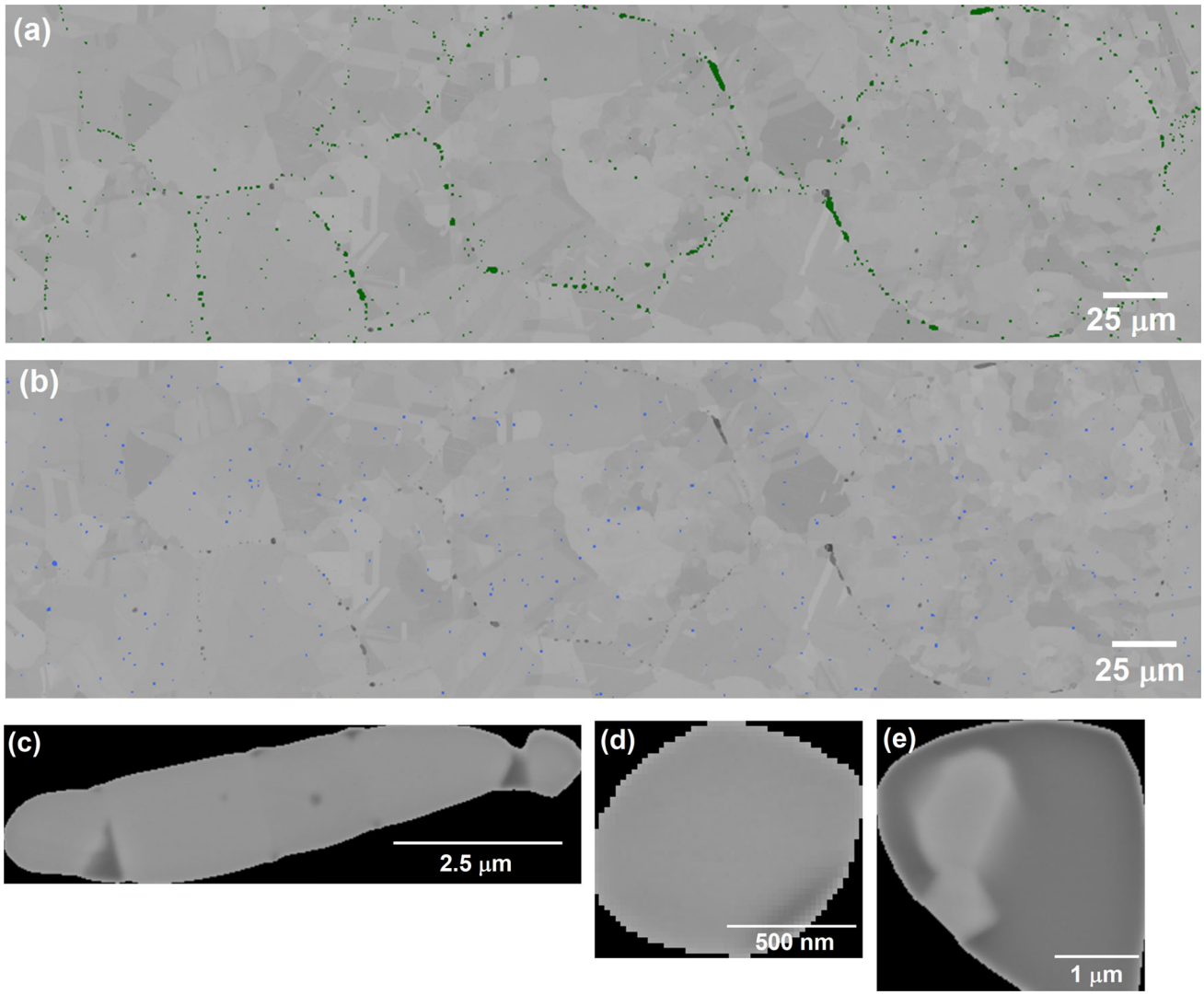

Fig. 7—Inclusions maps for the HIP'd 316L 106 to 150 μm sample showing (*a*) Cr-containing inclusions; (*b*) Cu-containing inclusions; and examples of specific inclusions: (*c*) a Cr-Mn-Ti-V-Si-containing oxide inclusion; (*d*) a Cr-Mn-Ti-V-containing oxide inclusion; and (*e*) a Cr-Mn-Ti-Si-Al oxysulfide inclusion.

sputtering. The data in supplementary Figure S-10 show that spectrum from the as-received powder is dominated by a broad main peak around 934 eV and satellite peaks indicative of Cu(II) species. After sputtering these Cu(II) compounds had been removed, resulting in a downward shift of the main Cu $2p_{3/2}$ component to 933 eV and the elimination of the satellite peaks, revealing a spectrum comprising approximately 60 wt pct Cu_2O and 40 wt pct Cu(0). This indicates that the Cu(II) compounds are at the surface initially but are easily removed under by ion beam.

In the aforementioned study by Hryha *et al.*,[16] Cr-Mn-Si-rich oxide particulates were reported on the surface of 316L steel powder. Supplementary Figure S-11 shows the Cr $2p_{3/2}$ and Si $2p$ regions from the three powders studied in this investigation, confirming the existence of Cr and Si oxides in all three powders in the as-received condition. The determination of the Cr oxidation state on the surface of metallic powders is of special importance for risk assessment on occupational health and safety in relation to hazardous substances.[30] The presence of Cr(III), and more

Table XIV. EDS Analysis (Weight Percent) from the Inclusions in Fig. 7

	O	Mn	Cr	Si	Fe	Ni	Al	Ti	V	N	C	S
(c)	23.0 ± 0.7	24.8 ± 0.8	34.2 ± 0.8	0.5 ± 0.1	5.0 ± 0.8			7.0 ± 0.3	0.7 ± 0.3	3.8 ± 0.9		
(d)	19.0 ± 0.5	21.3 ± 0.9	38.8 ± 1.0	0.7 ± 0.1	15.0 ± 1.0	2.1 ± 1.6		1.1 ± 0.2	0.7 ± 0.3		0.9 ± 0.2	0.3 ± 0.1
(e)	29.4 ± 0.5	26.1 ± 0.8	13.9 ± 0.6	12.9 ± 0.3	11.1 ± 0.9		1.1 ± 0.1	3.4 ± 0.3			1.1 ± 0.2	0.6 ± 0.1

importantly the absence of Cr(VI), on the surface oxides of the three powders of the present investigation has also been found on the surface of inert gas-atomized 316L powders < 45 μm and < 4 μm[30] and nitrogen gas-atomized 12Cr steel powder.[61]

D. *HIP'd 316L and 17-4PH Stainless Steels*

Exemplified inclusion analysis on the SEM images from the AMGA powder < 150 μm (Figure 4 and Table VIII) and VIGA powder 106 to 150 μm (Figure 5 and Table IX) to the two HIP'd conditions AMGA HIP'd < 150 μm (Figure 6 and Table XIII) and VIGA HIP'd 106 to 150 μm (Figure 7 and Table XIV) suggests that the larger globular inclusions in the HIP'd product were carried over from powder to the HIP'd product. Furthermore, Mn-Ti-(V)-Si-Al-containing inclusions in the 316L powder (see Figures 4 and 5 and Tables VIII and IX) can also evolve to two phases during HIP consolidation (Figures 6(c), 8, and 9). Close examination (Figure 8(b) and Table XV) also reveals an outer, single-phase shell of a Cr-Mn-Ti-(V)-Al-containing oxide and an inner core that consisted of a cluster of generally disconnected small particles (up to around 1 μm in size) of Cr-Mn-Ti-(V)-Al-containing oxides joined by a Mn-Ti-(V)-Al-containing glassy silicate phase. In practice, associations of coarse and complex inclusions may appear as an individual, single-phase inclusion when carrying out inclusion analysis on planar cross-sections.

In the aforementioned studies by Cooper *et al.*,[3,4] relatively fine (< 1 μm) and coarse (1 to 5 μm) non-metallic inclusions were analyzed by SE imaging in conjunction with EDS. Cr-Mn- (2 examples), Mn-Si- (2 examples), and Cr-Mn-Si-containing (1 example) oxide inclusions were reported in the HIP'd 316L steel.[4] From the point of view of trace impurity elements of Ti, Al, and Ca, Mn-Si-0.2Ti-(1 example), Mn-Si-0.4Ti-0.1Al-(1 example) and Mn-Si-0.3Ca-containing (1 example) were found in the 304L/316L steels.[3] Very limited data on compositional analysis of non-metallic inclusions in austenitic stainless steels are available with even less information reported on the presence of residual elements (no reported observations of Cu presence).

Figure 9 reveals another example of a coarse, two-phase non-metallic inclusion. The inclusion is formed of a cluster of disconnected particles (up to around 5 μm in size) of Cr-Mn-Ti-containing oxides ((V)-Al-free) joined by a Mn-(Ti)-containing glassy silicate phase ((V)-Al-free). However, in this case, the inclusion is triangular in shape. This suggests that the inclusion is located on the prior particle boundary (PPB) triple point, thus indicating some degree of plasticity. An analogy is the surface oxide cleaning by the field-assisted sintering technology (FAST) in which surface oxides can slide from PPBs to triple points.[62] Earlier work on hot-rolled austenitic stainless steel strip reported a complex, two-phase inclusion, which was composed of hard chromium galaxite phase (36MnO, 1FeO, $25Al_2O_3$, $39Cr_2O_3$) embedded in glassy manganese oxide-chromia-alumina-silica (23MnO, 1FeO,

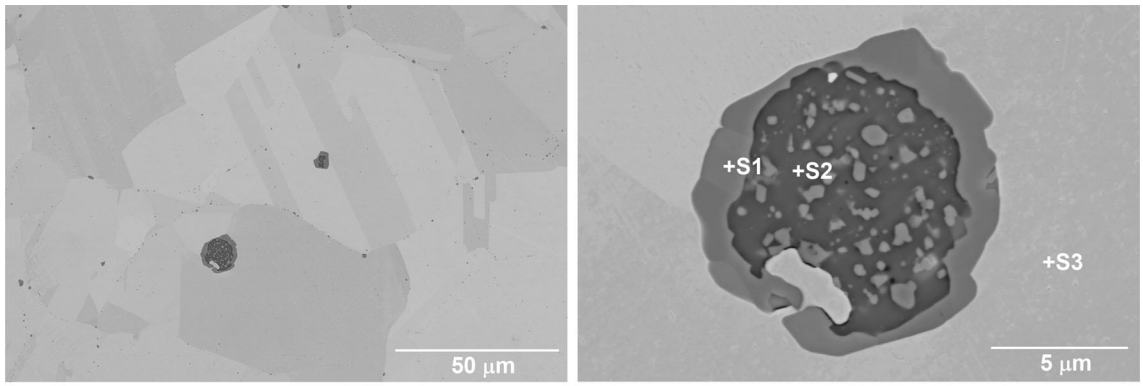

Fig. 8—BSE micrographs and EDS analysis of the AMGA HIP'd 316L < 150 μm sample showing (*a*) non-metallic inclusions and (*b*) detail of an outer, single-phase shell of a Cr-Mn-Ti-(V)-Al-containing oxide (S1) and an inner core that consisted of a cluster of generally disconnected small particles (up to around 1 μm in size) of Cr-Mn-Ti-(V)-Al-containing oxides joined by a Mn-Ti-(V)-Al-containing glassy silicate matrix (S2).

$43SiO_2$, $18Al_2O_3$, $4Cr_2O_3$, 8CaO).[63] The major similarities between the inclusion shown in Figure 29 of Reference 63 and the inclusion shown in Figure 9 are that both plastic silicate matrixes deform and both hard Cr-Mn-rich phases remained undeformed during steel deformation. The inclusion in Kiessling and Lange's work,[63] however, showed a greater degree of deformation than that of Figure 9. The globular, two-phase inclusion of Figure 8(b) would have resisted deformation during HIPping as the hard Cr-Mn-Ti-(V)-Al-containing oxide formed as a shell around the plastic silicate, as opposed to the non-shell inclusion of Figure 9.

For the AMGA HIP'd 316L < 150 μm sample, inclusions can be observed on the PPBs and within the particles (Figures 6(a) and (b)). The majority of the inclusions were found to be Ti-free Cr-Mn-rich, decreasing in the order: Cr Mn O S (19560 mm^{-2}) > Cr Mn O (6740 mm^{-2}) > Cr Mn S (2222 mm^{-2}) as quantified in Table III and in supplementary Figures S-1(d) and (e). It can also be seen in supplementary Figures S-1(d) and (e) that (i) in the *quasi*-absence of Ti retention in the inclusions, V is mainly retained in the two main type of inclusions above: Cr Mn V O S (521 mm^{-2}) and Cr Mn V O (150 mm^{-2}), and that (ii) residual Cu is mainly associated with Mn O S (1027 mm^{-2}) and Mn S (864 mm^{-2}), as opposed to Mn O (42 mm^{-2}).

For the VIGA HIP'd 316L 106 to 150 μm sample, the majority of the inclusions are located on the PPBs (Figures 7(a) and (b)). The majority of the inclusions were Cr-Mn-Ti-rich inclusions with and without V and decreased in the order of Cr Mn Ti O (1542 mm^{-2}) > Cr Mn Ti Si O (1378 mm^{-2}) > Cr Mn Ti Si O S (1030 mm^{-2}) as quantified in Table III and in supplementary Figures S-1(f) and (g). It can also be seen in supplementary Figures S-1(f) and (g) that, in the presence of Ti-containing inclusions, V is mainly associated with the following Cr-Mn-Ti-rich inclusions types: Cr Mn Ti V Al O oxides (390 mm^{-2}), Cr Mn Ti V O oxides (310 mm^{-2}), and Cr Mn Ti V Al O S oxysulfides (242 mm^{-2}). Higher N levels are also retained in the VIGA and HIP materials as compared to the AMGA and HIP materials (Tables I and II). Some examples of N-containing inclusions of the type of sulfides and oxysulfides are split in supplementary Figure S-1(g). Again, residual Cu is mainly associated with Mn O S (3579 mm^{-2}) and Mn S (1802 mm^{-2}), as opposed to Mn O (21 mm^{-2}).

The association of residual Cu with Mn S and Mn O S overwhelmingly outweighed that of Mn O in both HIP'd 316L samples (Table III). The smaller numbers of these particles fell in the size range 0 to 1 μm, representing most of the particles (Table V). Isolated examples of Cu Mn O S having a maximum dimension of up to 4 μm were observed (Table V). This association of residual Cu with Mn S and Mn O S has strategic implications for both Cu residual tolerance levels and standardization. Earlier work reported in Reference 64 showed that residual Cu (0.14 wt pct) has been found to combine

Table XV. EDS Analysis (Weight Percent) from the Inclusions in Fig. 8(b)

	O	Mn	Cr	Si	Fe	Ni	Al	Ti	V	N	C	Mo
S1	24.4 ± 0.2	24.0 ± 0.2	36.5 ± 0.2		1.5 ± 0.2		1.2 ± 0.0	3.7 ± 0.1	0.7 ± 0.1	5.5 ± 0.4	2.5 ± 0.1	
S2	32.2 ± 0.1	36.2 ± 0.2	11.3 ± 0.1	15.1 ± 0.1	1.3 ± 0.2		0.4 ± 0.0	0.9 ± 0.1	0.2 ± 0.1		2.4 ± 0.1	
S3		1.3 ± 0.1	15.6 ± 0.1	0.4 ± 0.0	65.9 ± 0.3	10.8 ± 0.4					4.1 ± 0.1	2.0 ± 0.1

with S (0.043 wt pct) to form CuS, which precipitates on existing MnS inclusions. More recently, a detailed review of metal oxysulfides was published by Larquet and Carenco,[65] in which it was reported that, Cu can form several oxysulfides such as $Cu_2O_{1-x}S_x$, $Sr_2Cu_2MnO_2S_2$, and Sr_2CuMO_3S (M = Sc, Cr, Fe).

From Table II for the Cu alloyed HIP'd 17-4PH steel, which had a very low S content of 0.0010 wt pct, it is clear that the formation of oxysulfides was suppressed and the formation of Cu O was much more favorable than the formation of Cu Mn O. The majority of these particles also fell in the smallest size range 0 to 1 μm, (Table VI).

E. *Standardization Implications*

Overall, these results have important implications for the development of standardization tools for residuals elements as well as cross-contamination for quality control of raw materials introduced in the supply chain as very small amounts of contamination can be identified in powders.

Note that, the level of residual Cu in powder 316L steel is not generally explicitly quoted in the literature[2–4,30,66–72] and other powder stainless steels,[68] for example AISI 304L[31] and 304.[66] A few examples in which the level of residual Cu was reported are 0.05-0.06 wt pct in HIP'd 316L,[5] 0.05 wt pct Cu in a water-atomized 316L powder[30] and 0.2 wt pct Cu in a gas-atomized 316L steel powder[51] and <0.1 wt pct in a 304L powder.[74,75] Sometimes, the chemical analysis is not specifically reported for a steel powder, but may be reported for the corresponding consolidated product, an example is a Cu residual value of 0.015 wt pct in AM AISI 304L.[76] Those Cu residual levels are generally less than half the value of 0.2 wt pct reported in Reference 33 that could be detrimental to the hot workability of the steel.

The aforementioned association of residual Cu with both Mn S and Mn O S in both HIP'd 316L steels of the present investigation suggests that residual levels of Cu <0.5 wt pct could be bound to both MnS and Mn O S inclusions in 316L steel for HIPping applications, ultimately leading to allowing an increased usage of steel scraps—containing high levels of Cu impurity—for powder atomization processes.

V. CONCLUSIONS

This paper empirically analyses how non-metallic inclusions evolved through processing from feedstock to powder and after HIP consolidation in Ti-V microalloyed 316L and Al-V microalloyed 17-4PH stainless steels. Using enhanced oxygen levels in the powders from powder handling, the evolution of non-metallic inclusions through processing has been documented. Consideration has also been made to determine the change in Ti, V, and Cu contents in both stainless steels. The main conclusions are as follows:

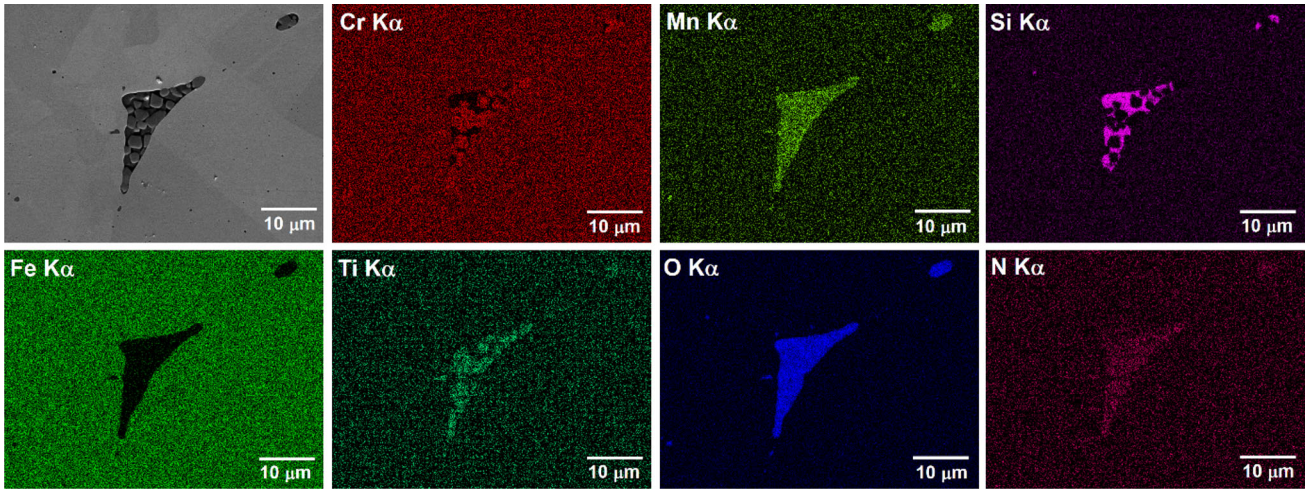

Fig. 9—Inclusion maps for the VIGA HIP'd 316L 106 to 150 μm sample.

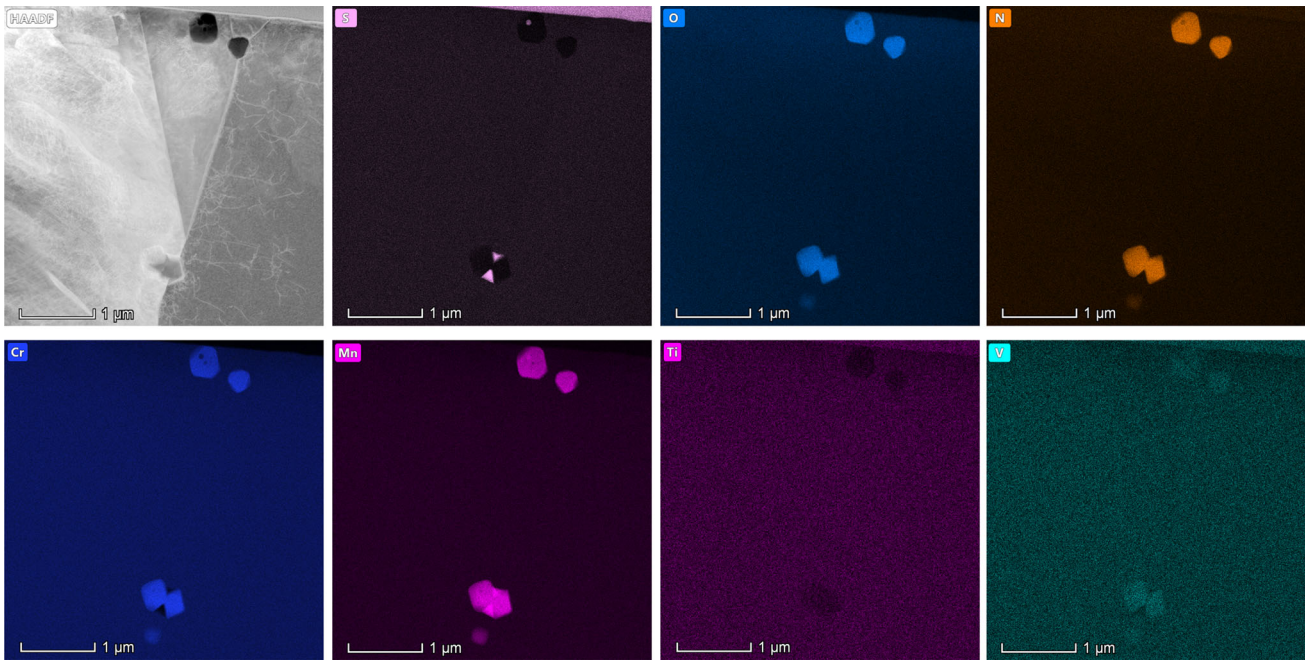

Fig. 10—TEM micrographs of the AMGA HIP'd 316L < 150 μm sample showing a HAADF-STEM image and EDXS elemental maps.

1. Microalloyed Ti was lost during air melting but partly retained after vacuum melting leading to the presence of fine and complex Ti-containing precipitates. Microalloyed V was retained in the melt by the use of both AMGA and VIGA processes, and therefore available for precipitation during HIPping. Residual Cu was retained during both air and vacuum melting and was associated with Mn S and Mn O S inclusions overwhelmingly outweighing that of simple Mn O in the two HIP'd 316L samples.
2. There were significant differences between the dominant types of inclusions through processing in Ti-V microalloyed 316L and Al-V microalloyed 17-4PH stainless steels. These were

Mn Ti N S (TiN/MnS) for the 316L steel feedstock; Mn Ti Si Al oxides in the 316L < 150 μm powder; Ti Si Al oxides for the 316L 106 to 150 μm powder: Ti-free Cr-Mn-rich oxides, sulfides, and oxysulfides for the HIP'd 316L < 150 μm steel and both Cr-Mn-Ti-(V)-rich oxides and oxysulfides in the HIP'd 316L 106 to 150 μm steel.

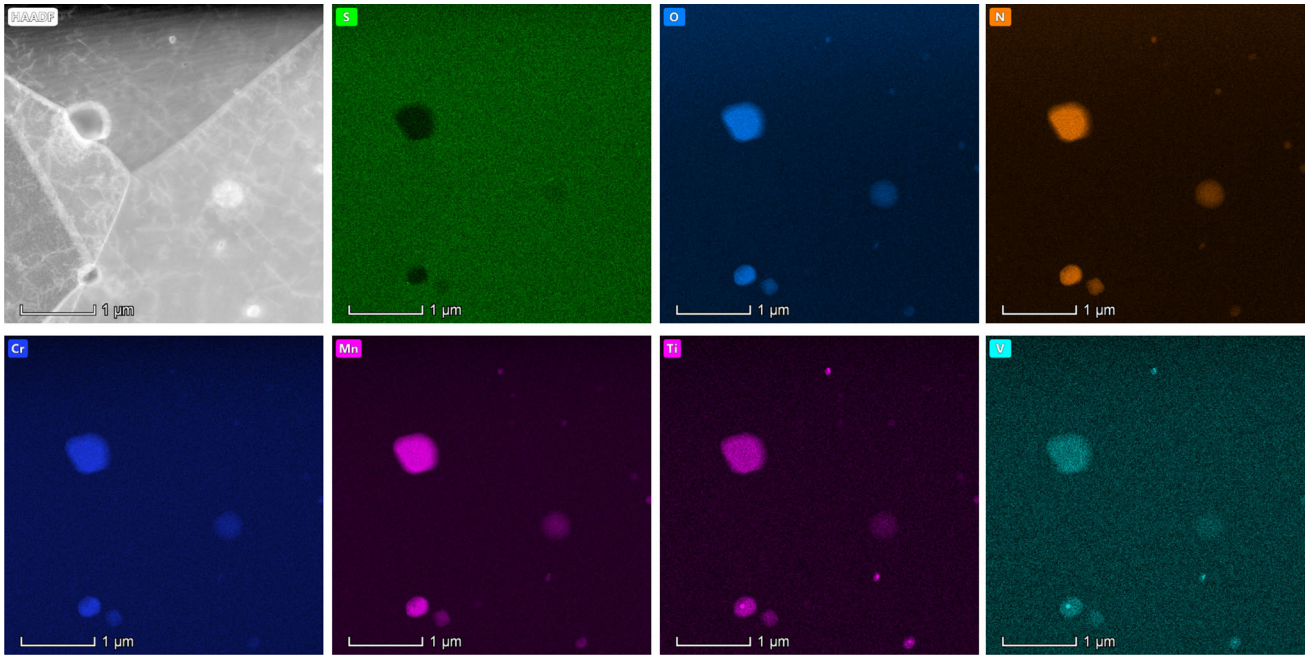

Fig. 11—TEM micrographs of the VIGA HIP'd 316L 106 to 150 μm sample showing a HAADF-STEM image and EDXS elemental maps.

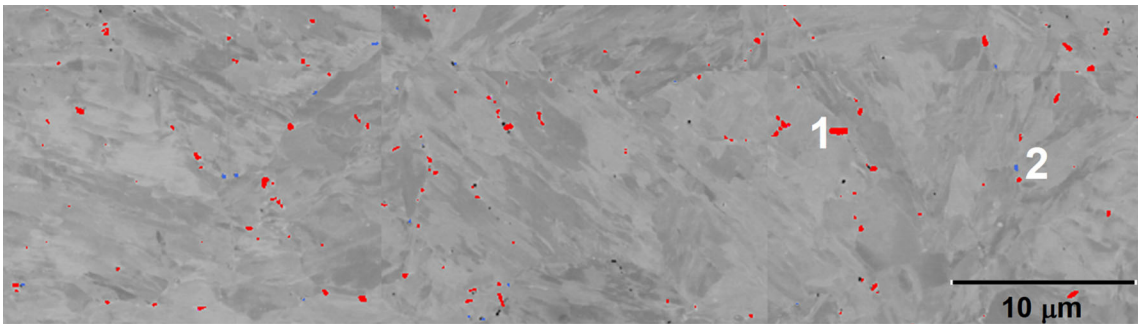

Fig. 12—Phase map for the VIGA HIP'd 17-4PH 25 to 45 μm sample showing Nb-Cr-V-Cu-containing (red 1) and Cu-rich (blue 2) phases (Color figure online).

Table XVI. EDS Analysis (Weight Percent) from the Phases in Fig. 12

Phase	Nb	Cr	Fe	N	V	Cu	Ni	Mo	C
1	37.8 ± 0.6	27.7 ± 0.5	25.7 ± 0.6	4.9 ± 0.3	2.0 ± 0.2	1.2 ± 0.2	0.4 ± 1.0	0.3 ± 0.4	
2		6.8 ± 0.3	27.6 ± 0.5			62.5 ± 0.5		0 ± 0.2	3.0 ± 0.2

Isolated examples of inclusions were observed for both 17-4PH steel feedstock (0.0009S-0.0010O-0.030N (wt pct)) and powder (0.0010S-0.0318O-0.0351N (wt pct)) but in insufficient number to be significant, suggesting that in the powder sample, oxygen was mainly present in the form of surface oxides. Low-Cr oxides without Nb, Ti, and V were the dominant inclusion type for the HIP'd 25 – 45 μm sample that had a very low sulfur content of 0.0010 wt pct and an oxygen content of 0.0216 wt pct, and therefore exhibited the lowest number density of sulfides and oxysulfides compared to the two HIP'd 316L samples.

3. The Ti content in the 316L steel varied from 0.13 wt pct Ti in the feedstock to low residual levels in the AMGA samples: <0.02 wt pct Ti in the powder and <0.005 wt pct Ti in the HIP'd < 150 μm sample, whereas it was partly retained to relatively high

levels in the VIGA samples: 0.046 wt pct Ti in the powder and 0.05 wt pct in the HIP´d 106 to 150 μm sample. In the latter case, Ti-rich precipitates were observed by HAADF-STEM in conjunction with EDX to provide pinning of grain boundaries, resulting in a smaller mean austenite grain size value of 17.3 ± 15.4 compared with 23.1 ± 21.6 for the AMGA HIP'd < 150 μm sample.

4. XPS analysis revealed the presence of many different elements in their metallic and oxidized compounds, within the three steel powders examined (VIGA 316L 106 to 150 μm, VIGA 316L 15 to 45 μm, and 17-4PH 106 to 150 μm). The common peaks in all three samples were Fe 2*p*—Fe(0), FeO and Fe_2O_3; Cr 2*p*—Cr(0) and Cr(III); Si 2*p*—Si(0) and SiO; O 1*s* and C 1*s*; with common peaks only for the two 316L powders Si 2*p*—SiO_2; Mo 3*d*—Mo(0) and MoO_3; Ni 2*p*—Ni(0) and Ni(II) and Mn 2*p*—Mn (0) and MnO and with particular peaks for the 316L 106 – 150 μm powder Ti 2*p*—Ti(0) and TiO_2; with particular peaks for the 17-4PH 106 – 150 μm powder Sn 3*d*—Sn(0) and SnO/SnO_2; N 1s and Nb 3*d*—Nb(0), NbO_2, NbC/NbN; P 2*p*—P(0) and phosphates and Cu 2*p*—Cu(II) in the as-received condition only, but both Cu_2O and Cu(0) after Ar^+ sputtering only.
5. A thin oxide film formed on the powder surface, thicker for the 316L powder than the 17-4PH powder as indicated by XPS analysis of selected powder precursors.

ACKNOWLEDGMENTS

The financial support of Liberty Powder Metals is gratefully acknowledged. This work was carried out as part of the UK government's Advanced Manufacturing Supply Chain Initiative (AMSCI) - CASCADE project.

OPEN ACCESS

ELECTRONIC SUPPLEMENTARY MATERIAL

The online version of this article (https://doi.org/10.1007/s11661-020-06010-w) contains supplementary material, which is available to authorized users.

REFERENCES

1. *Stainless Steels*, 2nd ed., J.R. Davis, ed., *Stainless Steels*, ASM Speciality Handbook. ASM International, Materials Park, OH, 1994.
2. S. Irukuvarghula, H. Hassanin, C. Cayron, M.M. Attallah, D. Stewart and M. Preuss *Acta Mater*., 2017, vol. 133, pp. 269–81.
3. A.J. Cooper, N.I. Cooper, A. Bell, J. Dhers, and A.H. Sherry: *Metall. Mater. Trans. A*, 2015, vol. 46A (11), pp. 5126–38.
4. A.J. Cooper, N.I. Cooper, A. Bell, J. Dhers, and A.H. Sherry: *Metall. Mater. Trans. A*, 2016, vol. 47A (9), pp. 4467–75.
5. A.J. Cooper, W.J. Brayshaw, and A.H. Sherry: *Metall. Mater. Trans. A*, 2018, vol. 49A (5), pp. 2018–79.
6. U. Engström and E. Schneider: in *World Congress on Powder Metallurgy, Proceedings of World PM2018, Beijing, China*, 16–20 September 2018, pp. 43–52.
7. V. Polard and B. Blitz: in *World Congress on Powder Metallurgy, Proceedings of World PM2018, Beijing, China*, 16–20 September 2018, pp. 1152–55.
8. R. Goto: in *World Congress on Powder Metallurgy, Proceedings of World PM2018, Beijing, China*, 16–20 September 2018, pp. 1979–82.
9. P. Gundermann: in *Euro PM2018 Plenary presentation, Bilbao, Spain*, 14–18 October 2018. https://www.europm2018.com/onsite-content-access. Accessed 24 June 2020.
10. P. Bajaj, A. Hariharan, A. Kini, P. Kürnsteiner, D. Raabe, and E.A. Jägle: *Mater. Sci. Eng. A*, 2020, vol. 772, p. 138633.
11. N. Li, S. Huang, G. Zhang, R. Qin, W. Liu, H. Xiong, G. Shi, and J. Blackburn: *J. Mater. Sci. Technol.*, 2019, vol. 35 (2), pp. 242–69.
12. H. Fayazfar, M. Salarian, A. Rogalsky, D. Sarker, P. Russo, V. Paserin, and E. Toyserkani: *Mater. Des.*, 2018, vol. 144, pp. 98–128.
13. J. Dawes, R. Bowerman, and R. Trepleton: *Johnson Matthey Technol. Rev.*, 2015, vol. 59 (3), pp. 243–56.
14. H. Men and Z. Fan: *Mater. Sci. Technol.*, 2011, vol. 27 (6), pp. 1033–39.
15. H.J.T. Ellingham: *J. Soc. Chem. Ind.*, 1944, vol. 63, pp. 125–33.
16. E. Hryha, R. Shvab, H. Gruber, A. Leicht and L. Nyborg: in *Euro PM2017 Proceedings, Milan, Italy*, 1–5 October 2017.
17. M.J. Balart, X. Hao, S. Marks, G.D. West, M. Strangwood and C.L. Davis: in *World Congress on Powder Metallurgy, Proceedings of World PM2018, Beijing, China*, 16–20 September 2018, pp. 86–91.
18. M.J. Balart, H.G.C. Hamilton, X. Hao, M. Strangwood and C.L. Davis: in *Euro PM2018 Proceedings*, 14–18 October, Bilbao, Spain.
19. Y. Sun, R.J. Hebert, and M. Aindow: *Mater. Des.*, 2017, vol. 140, pp. 153–62.
20. M. Nuspl, W. Wegscheider, J. Angeli, W. Posch, and M. Mayr: *Anal. Bioanal. Chem.*, 2004, vol. 379, pp. 640–45, https://doi.org/10.1007/s00216-004-2528-y.
21. B. Goulart Bartosiaki, J.A. Morales Pereira, W. Viana Bielefeldt and A.C. Faria Vilela: *J. Mater. Res. Technol.*, 2015, vol. 4 (3), pp. 235–40.
22. E. Santecchia, P. Mengucci, A. Gatto, E. Bassoli, L. Denti, F. Bondioli and G. Barucca: in *Euro PM2018 Proceedings, Bilbao, Spain*, 14–18 October 2018.
23. E. Santecchia, P. Mengucci, A. Gatto, E. Bassoli, S. Defanti, and G. Barucca: *Materials*, 2019, vol. 12, p. 2342, https://doi.org/10.3390/ma12152342.
24. T.F. Murphy, C.T. Schade and A. Zwiren (2018): *Int. J. Powder Metall.*, 2018, vol. 54 (1), pp. 47–59.
25. P. Kaushik, J. Lehmann, and M. Nadif: *Metall. Mater. Trans. B*, 2012, vol. 43B (4), pp. 710–25.

26. P. Kaushik, H. Pielet, and H. Yin: *Ironmaking Steelmaking*, 2009, vol. 36 (8), pp. 561–71, https://doi.org/10.1179/030192309X12492910938131.
27. P. Kaushik, H. Pielet, and H. Yin: *Ironmaking Steelmaking*, 2009, vol. 36 (8), pp. 572–82, https://doi.org/10.1179/030192309X12492910938177.
28. A.D. Brandão, R. Gerard, J. Gumpinger, S. Beretta, A. Makaya, L. Pambaguian, and T. Ghidini: *Materials*, 2017, vol. 10, p. 522, https://doi.org/10.3390/ma10050522.
29. E. Klar and P.K. Samal: *Powder Metallurgy Stainless Steels: Processing, Microstructures, and Properties*, ASM International, Materials Park, OH, 2007, pp. 30–32. https://books.google.co.uk/books?isbn=1615030522. Accessed 12 Nov 2018.
30. Y. Hedberg, M. Norell, J. Hedberg, P. Szakálos, P. Linhardt and I. Odnevall Wallinder: *Powder Metall.*, 2013, vol. 56 (2), pp. 158–63.
31. A.J. Cooper, W.J. Brayshaw, and A.H. Sherry: *Metall. Mater. Trans. A*, 2018, vol. 49A (3), pp. 811–16.
32. H. Ohno, K. Matsubae, K. Nakajima, Y. Kondo, S. Nakamura, Y. Fukushima, and T. Nagasaka: *Environ. Sci. Technol.*, 2017, vol. 51 (22), pp. 13086–94.
33. H. Katayama, N. Sano, M. Sasabe, and S. Matsuoka: *Scand. J. Metall.*, 1998, vol. 27 (1), pp. 24–30.
34. P.C. Rem, F. van den Broeck, and M.C.M. Bakker: *Ironmaking Steelmaking*, 2012, vol. 39 (7), pp. 504–07, https://doi.org/10.1179/1743281212Y.0000000017.
35. J.K.S. Tee and D.J. Fray: *Ironmaking Steelmaking*, 2006, vol. 33 (1), pp. 19–23, https://doi.org/10.1179/174328106X80028.
36. M.B. Mesina, T.P.R. de Jong, and W.L. Dalmijn: *Int. J. Miner. Process.*, 2005, vol. 76, pp. 21–31.
37. C.Y. Chen, C.H. Li, T.C. Tsao, P.H. Chiu, S.P. Tsai, J.R. Yang, L.J. Chiang, and S.H. Wang: *Mater. Today Commun.*, 2020, vol. 23, art. no. 100895.
38. A.M. Sage: in *Fundamentals of Microalloying Forging Steels*. Ed. G. Krauss and S.K. Banerji, AIME, 1987, pp. 239–53.
39. H. Wei, Y.L. Chen, W. Yu, L. Su, X. Wang, and D. Tang: *Construct. Build. Mater.*, 2020, vol. 239 (117815), pp. 1–13.
40. K.H. Lo, C.H. Shek and J.K.L. Lai. *Mater. Sci. Eng., R*, 2009, vol. 65 (4–6), pp. 39–104.
41. M.J. Konstantinović, I. Uytdenhouwen, G. Bonny, N. Castin, L. Malerba, and P. Efsing: *Acta Mater.*, 2019, vol. 179, pp. 183–89.
42. G.R. Odette, T. Yamamoto, T.J. Williams, R.K. Nanstad, and C.A. English: *J. Nucl. Mater.*, 2019, vol. 526 (151863), pp. 1–38.
43. N. Almirall, P.B. Wells, T. Yamamoto, K. Wilford, T. Williams, N. Riddle, and G.R. Odette: *Acta Mater.*, 2019, vol. 179, pp. 119–28.
44. B. Mintz: *ISIJ Int.*, 1999, vol. 39 (9), pp. 833–55.
45. Å. Bergman and R. West: *Scr. Metall.*, 1988, vol. 22 (5), pp. 659–63.
46. S.A.E. Aerospace, *Aerospace Material Specification: AMS 5662*, SAE International 2009.
47. K. Kandasamy, O. Messe, S. Foster, S. Kelly and S. Sharma: in *Euro PM2018 Proceedings, Bilbao, Spain*, 14–18 October 2018.
48. ASTM A542 / A542M-19, *Standard Specification for Pressure Vessel Plates, Alloy Steel, Quenched-and-Tempered, Chromium-Molybdenum, and Chromium-Molybdenum-Vanadium*, ASTM International, West Conshohocken, PA, 2019, www.astm.org.
49. ASTM A508 / A508M-18, *Standard Specification for Quenched and Tempered Vacuum-Treated Carbon and Alloy Steel Forgings for Pressure Vessels*, ASTM International, West Conshohocken, PA, 2018, www.astm.org.
50. ASTM A988 / A988M-17: *Standard Specification for Hot Isostatically-Pressed Stainless Steel Flanges, Fittings, Valves, and Parts for High Temperature Service*, ASTM International, West Conshohocken, PA, 2017, www.astm.org.
51. N.P. Lavery, J. Cherry, S. Mehmood, H. Davies, B. Girling, E. Sackett, S.G.R. Brown, and J. Sienz: *Mater. Sci. Eng. A*, 2017, vol. 693, pp. 186–213.
52. Y. Sun, R. Hebert, and M. Aindow: *Mater. Des.*, 2018, vol. 156, pp. 429–40.
53. N. Fairley, *Fairley*, http://www.casaxps.com, ©Casa software Ltd., 2018.
54. M.J. Balart, C.L. Davis, and M. Strangwood: *Mater. Sci. Eng. A*, 2000, vol. 284 (1–2), pp. 1–13.
55. X. Hao, R. Aswathenarayanaswamy, S. Christie, M.J. Balart, and C.L. Davis: *´Cracking in additive manufactured 316L stainless steel´, AAMS 2018, 3–4 Sept*, Sheffield, UK, 2018.
56. M.J. Balart, X. Hao, S. Marks, G.D. West and C.L. Davis: in *Euro PM2019 Proceedings, Maastricht, The Netherlands*, 13–16 October 2019.
57. M.J. Heiden, L.A. Deibler, J.M. Rodelas, J.R. Koepke, D.J. Tung, D.J. Saiz, and B.H. Jared: *Addit. Manuf.*, 2019, vol. 25, pp. 84–103.
58. M.C. Biesinger, B.P. Payne, A.P. Grosvenor, L.W.M. Lau, A.R. Gerson and R. St. C. Smart: *Appl. Surf. Sci.*, 2011, vol. 257 (7), pp. 2717–30.
59. A. Leicht, R. Shvab, E. Hryha, L. Nyborg and L.E. Rännar: in *7th Int. Swedish Production Symposium* (Lund; Sweden; 25–27 October 2016).
60. M. Norell, L. Nyborg, and M. Friesel: *Powder Metall.*, 1998, vol. 41 (1), pp. 31–39.
61. L. Nyborg, M. Norell, and I. Olefjord: *Surf. Interface Anal.*, 1992, vol. 19 (1–12), pp. 607–14.
62. M. Wu, Y. Yang, G. Yang, K. Huang, and D. Yin: *J. Alloys Compd.*, 2019, vol. 784, pp. 975–79.
63. R. Kiessling and N. Lange: *Non-metallic inclusions in steel. Part I*, Iron and Steel Institute, London, UK, 1964.
64. I. Madariaga and I. Gutiérrez: *Scripta Mater.*, 1997, vol. 37 (8), pp. 1185–92.
65. C. Larquet and S. Carenco: *Front. Chem.*, 2020, vol. 8, article 179, https://doi.org/10.3389/fchem.2020.00179.
66. A.S. Wu, D.W. Brown, M. Kumar, G.F. Gallegos, and W.E. King: *Metall. Mater. Trans. A*, 2014, vol. 45A (13), pp. 6260–70.
67. Y. Hedberg, O. Karlsson, P. Szakalos, and I.O. Wallinder: *Mater. Lett.*, 2011, vol. 65 (14), pp. 2089–92.
68. C. Pauzon, E. Hryha, P. Forêt, and L. Nyborg: *Mater. Des.*, 2019, vol. 179, p. 107873, https://doi.org/10.1016/j.matdes.2019.107873.
69. A. Leicht, U. Klement, and E. Hryha: *Mater. Charact.*, 2018, vol. 143, pp. 137–43.
70. A. Leicht, M. Rashidi, U. Klement, and E. Hryha: *Mater. Charact.*, 2020, vol. 159, p. 110016.
71. P. Quinn, S. O'Halloran, J. Lawlor, and R. Raghavendra: *Adv. Mater. Process. Technol.*, 2019, vol. 5 (2), pp. 348–59, https://doi.org/10.1080/2374068X.2019.1594602.
72. A. Röttger, K. Geenen, M. Windmann, F. Binner and W Theisen: *Mater. Sci. Eng., A*, 2016, vol. 678, pp. 365–76.
73. J. Yu, M. Rombouts, and G. Maes: *Mater Des.*, 2013, vol. 45, pp. 228–35.
74. A.T. Sutton, C.S. Kriewal, M.C. Leu, J.W. Newkirk, and B. Brown: *Addit. Manuf.*, 2020, vol. 31, p. 100904.
75. A.T. Sutton, C.S. Kriewall, S. Karnati, M.C. Leu, and J.W. Newkirk: *Addit. Manuf.*, 2020, vol. 32, p. 100981.
76. V. Laghi, M. Palermo, L. Tonelli, G. Gasparini, L. Ceschini, and T. Trombetti: *Int. J. Adv. Manuf. Technol.*, 2020, vol. 106, pp. 3693–705.